

1

# Snow Interception Relationships with 2 Meteorology and Canopy Structure in a 3 Subalpine Forest

4

5 **Authors:**

6 A. Cebulski<sup>1</sup> (ORCID ID - 0000-0001-7910-5056)

7 J.W. Pomeroy<sup>1</sup> (ORCID ID - 0000-0002-4782-7457)

8 <sup>1</sup>Centre for Hydrology, University of Saskatchewan, Canmore, Canada

9 **Corresponding Author:** A. Cebulski, alexcebulski@gmail.com

10 **Abstract:** Snow accumulation models differ in how snow interception and ablation processes  
11 are represented and thus their application to diverse climates and forest types is uncertain.  
12 Existing parameterizations of initial snow interception before unloading include inherently cou-  
13 pled canopy snow accumulation and ablation processes. This leads to difficulty in diagnosing  
14 processes and adding possible errors to simulations when incorporated as canopy intercep-  
15 tion routines in models that already account for canopy snow ablation. This study evaluates  
16 the theory underpinning these parameterizations using high-temporal resolution and fine-scale  
17 measurements of throughfall for events with minimal snow ablation and redistribution in both  
18 the canopy and on the ground. The relationship between these throughfall measurements,  
19 event meteorology, and a novel lidar-based measurement of canopy structure are assessed in  
20 two subalpine forest plots in the Canadian Rockies. Contrary to existing theories, no as-  
21 sociation of canopy snow load or air temperature with interception efficiency was observed.

Instead, canopy structure emerged as the primary factor governing snow accumulation. A wind-driven snowfall event demonstrated that non-vertical hydrometeor trajectories can significantly increase snow-leaf contact area, thereby enhancing initial interception before ablation. Prediction of interception efficiency for this event improved dramatically when adjusted for hydrometeor trajectory angle based on a wind speed at one-third of the canopy height. Snow-leaf contact area showed a high sensitivity to wind speed, increasing by up to 95% with a  $1 \text{ m s}^{-1}$  wind speed. The study proposes a new parameterization that calculates throughfall, independent of processes that ablate snow from the canopy, as a function of snow-leaf contact area adjusted for hydrometeor trajectory angle. This new parameterization successfully estimated subcanopy snow accumulation for a snowfall event at two forest plots measured using lidar and snow surveys. By separating canopy snow ablation from snow interception processes, this new model offers potentially improved prediction of subcanopy snow accumulation when combined with canopy snow ablation parameterizations.

**Keywords:** snow interception, throughfall, ablation, forest, snowpack, lidar, process-based modelling

## 1 Introduction

Over half of North America's snow-covered zone is covered by forests (Kim et al., 2017), significantly impacting the accumulation and redistribution of snowpacks and subsequent snowmelt runoff. Essery et al. (2003) estimated that 25–45% of annual snowfall may be lost to the atmosphere due to sublimation of snow intercepted in forest canopies globally. Snow intercepted in the canopy can sublimate and melt at much higher rates than the subcanopy snowpack (Floyd, 2012; Lundberg & Hallidin, 1994; Pomeroy et al., 1998), reducing the amount of snow available for runoff. Vegetation structure is one of the primary factors controlling the partitioning of snowfall into throughfall and interception, and thus governs the quantity of snow subject to sublimation from the canopy (Hedstrom & Pomeroy, 1998; Storck et al., 2002). However, forest thinning efforts aimed at limiting sublimation losses to increase snowmelt runoff do not

48 always lead to a corresponding increase in spring streamflow (Golding & Swanson, 1978; Har-  
49 pold et al., 2020; Pomeroy et al., 2012; Troendle, 1983). This may be due to increased ablation  
50 rates when forest cover is reduced, desynchronization of snowmelt, and sub-surface hydrology  
51 interactions (Ellis et al., 2013; Musselman et al., 2015; Pomeroy et al., 1997; Safa et al., 2021;  
52 Varhola et al., 2010). Due to the significant impact of forest cover on snow accumulation and  
53 ablation, and sparse or absent monitoring networks for subcanopy snow accumulation (Rittger  
54 et al., 2020; Vionnet et al., 2021), land management, ecological conservation and water re-  
55 source decisions rely on robust models of snow redistribution to estimate past, current and  
56 future subcanopy snowpacks.

57 Hedstrom & Pomeroy (1998), working in the cold continental boreal forest, proposed that  
58 initial snow interception efficiency was controlled by the maximum canopy load which itself  
59 was a function of leaf area index and air temperature. Unloading was found to be an expo-  
60 nential function of time and observed only days or weeks after the interception event. Storck  
61 et al. (2002), working in temperate coastal forests, emphasized the role of air temperature  
62 in controlling the maximum canopy snow load. Gelfan et al. (2004) demonstrated accurate  
63 subcanopy snowpack simulations at study sites in Russia by treating the Hedstrom & Pomeroy  
64 (1998) and Storck et al. (2002) parameterizations separately while using a step-based function  
65 to choose either parameterization based on temperature. A similar parameterization in the  
66 Cold Regions Hydrological Model (Pomeroy et al., 2022) has shown strong performance at  
67 sites across Canada, northern United States, Switzerland, and Spain. However, overestima-  
68 tion of subcanopy snow accumulation was reported by Lundquist et al. (2021) and Lumbrazo  
69 et al. (2022) when combining the Hedstrom & Pomeroy (1998) routine with ablation pa-  
70 rameterizations from different studies (e.g., Roesch et al., 2001). The coupling of ablation  
71 processes within existing snow interception models (Hedstrom & Pomeroy, 1998; Storck et  
72 al., 2002) may contribute to overestimates of throughfall, canopy snow unloading, and canopy  
73 snow melt when combined with other canopy snow ablation parameterizations. Additional  
74 observations of snow interception that exclude ablation processes could help determine the  
75 applicability of the interception theories proposed by Hedstrom & Pomeroy (1998) and Storck

76 et al. (2002). Hedstrom & Pomeroy's (1998) theory also suggests that moderate wind speeds,  
77 which can result in more horizontal hydrometeor trajectories and increase the snow-leaf con-  
78 tact area and interception efficiency at the plot scale. This association has also been shown in  
79 rainfall interception studies to decrease throughfall of rain (Herwitz & Slye, 1995; Van Stan  
80 et al., 2011). Despite this importance for rainfall, the relationship proposed by Hedstrom &  
81 Pomeroy (1998), has typically not been included in snow accumulation models (Clark et al.,  
82 2020; Mahat & Tarboton, 2014) and empirical testing of this relationship is lacking.

83 The objective of this paper is to evaluate the theories underlying existing snow interception  
84 models using high spatial and temporal resolution measurements of subcanopy snow accumu-  
85 lation for events with minimal canopy snow ablation. These new observations are investigated  
86 to address the following research questions:

- 87 1. Are the existing theories regarding the relationships between meteorology and forest  
88 structure and snow interception supported by in-situ observations?
- 89 2. Is snow interception influenced by non-vertical hydrometeor trajectory angles over a  
90 wind-driven snowfall event?
- 91 3. To what extent can these findings inform the development of a new parameterization for  
92 snow interception?

## 93 **2 Theory**

### 94 **2.1 Snow Interception**

95 The canopy snow load,  $L$  ( $\text{kg m}^{-2}$ ) can be estimated from the mass balance:

$$\frac{dL}{dt} = q_{sf} - q_{tf} - q_{unld} - q_{drip} - q_{wind}^{veg} - q_{sub}^{veg} \quad (1)$$

96 where  $q_{sf}$  is the snowfall rate ( $\text{kg m}^{-2} \text{s}^{-1}$ ),  $q_{tf}$  is the throughfall rate ( $\text{kg m}^{-2} \text{s}^{-1}$ ),  $q_{unld}$  is the  
 97 canopy snow unloading rate ( $\text{kg m}^{-2} \text{s}^{-1}$ ),  $q_{drip}$  is the canopy snow drip rate due to canopy  
 98 snowmelt ( $\text{kg m}^{-2} \text{s}^{-1}$ ),  $q_{wind}^{veg}$  is the wind transport rate in or out of the control volume ( $\text{kg m}^{-2}$   
 99  $\text{s}^{-1}$ ), and  $q_{sub}^{veg}$  is the intercepted snow sublimation rate ( $\text{kg m}^{-2} \text{s}^{-1}$ ).

100 During periods with low air temperatures and low wind speeds,  $q_{unld}$ ,  $q_{drip}$ ,  $q_{wind}^{veg}$ , and  $q_{sub}^{veg}$   
 101 can be assumed negligible. Interception efficiency,  $\frac{I}{P}$  (-), which is the fraction of snowfall  
 102 intercepted over  $\Delta t$  before ablation, can then be calculated during these periods as:

$$\frac{I}{P} = \frac{\Delta L}{q_{sf} \Delta t} \quad (2)$$

103 and throughfall,  $q_{tf}$  can be calculated as:

$$q_{tf} = \left(1 - \frac{I}{P}\right) \cdot q_{sf} \quad (3)$$

## 104 2.2 Hydrometeor Trajectory Angle

105 The trajectory angle,  $\theta_h$  of a hydrometeor as the departure in degrees ( $^\circ$ ) from a vertical plane,  
 106 is shown in Herwitz & Slye (1995) to be calculated as:

$$\theta_h = \arctan\left(\frac{x_h(u_z)}{v_h(D_h)}\right) * \frac{180}{\pi} \quad (4)$$

107 where  $v_h(D_h)$  is the terminal fall velocity of the hydrometeor ( $\text{m s}^{-1}$ ), which is a function of  
 108 the hydrometeor diameter,  $D_h$  and  $x_h(u_z)$  is the horizontal velocity of the hydrometeor ( $\text{m}$   
 109  $\text{s}^{-1}$ ) which is a function of the within canopy wind speed,  $u_z$  at height above ground,  $z$ . This  
 110 assumes the hydrometeors are following fluid points in the atmosphere.

<sub>111</sub> **3 Data and Methods**

<sub>112</sub> **3.1 Study Site**

<sub>113</sub> This study was conducted at Fortress Mountain Research Basin (FMRB), Alberta, Canada,  
<sub>114</sub> -115° W, 51° N, a continental headwater basin in the Canadian Rockies (Figure 1). Data from  
<sub>115</sub> this study was collected between October 2021 and July 2023 within and surrounding two  
<sub>116</sub> forest plots adjacent to the FMRB Powerline Station (PWL) and Forest Tower Station (FT)  
<sub>117</sub> at ~2100 m above sea level as shown in Figure 1. The average annual precipitation at PWL  
<sub>118</sub> Station from 2013 to 2023 was 1045 mm, with the peak annual snow water equivalent (SWE)  
<sub>119</sub> reaching 465 kg m<sup>-2</sup>, typically occurring in late April. The PWL and FT forest plots include  
<sub>120</sub> discontinuous stands of 70% subalpine fir (*Abies lasiocarpa*) and 30% Engelmann spruce (*Picea*  
<sub>121</sub> *engelmannii*) (Langs et al., 2020). The PWL plot is located 120 m to the northwest of FT  
<sub>122</sub> station and contains a forest clearing with a diameter of ~12 m, surrounded by a closed canopy.  
<sub>123</sub> The canopy coverages of the two forest plots are 0.51 and 0.29 and the winter leaf area indices  
<sub>124</sub> are 2.07 and 1.66 for PWL and FT respectively. The average height of the canopy surrounding  
<sub>125</sub> the plot to the east of the PWL station is 10.5 m and surrounding the forest plot around the  
<sub>126</sub> FT Station is 7.1 m. The forest of the FT plot has a discontinuous canopy without artificial  
<sub>127</sub> clearings. In August of 1936, the majority of vegetation in FMRB burned during a large forest  
<sub>128</sub> fire that affected most of the Kananaskis Valley (Fryer et al., 1988). Following the fire, the  
<sub>129</sub> forest within the PWL and FT forest plots has naturally regenerated, though some trees have  
<sub>130</sub> been removed for road clearing and creation of a snow study plot.

<sub>131</sub> **3.2 Meteorological Measurements**

<sub>132</sub> Measurements of air temperature and relative humidity (Vaisala model HMP155A), wind speed  
<sub>133</sub> and direction (RM Young model 86000 2-D ultrasonic anemometer) were made 4.3 m above  
<sub>134</sub> the ground at FT station (Figure 1). Wind speed measurements from a 3-cup anemometer  
<sub>135</sub> (Met One model 014A), installed adjacent to the 2-D ultrasonic anemometer at 4.3 m, were

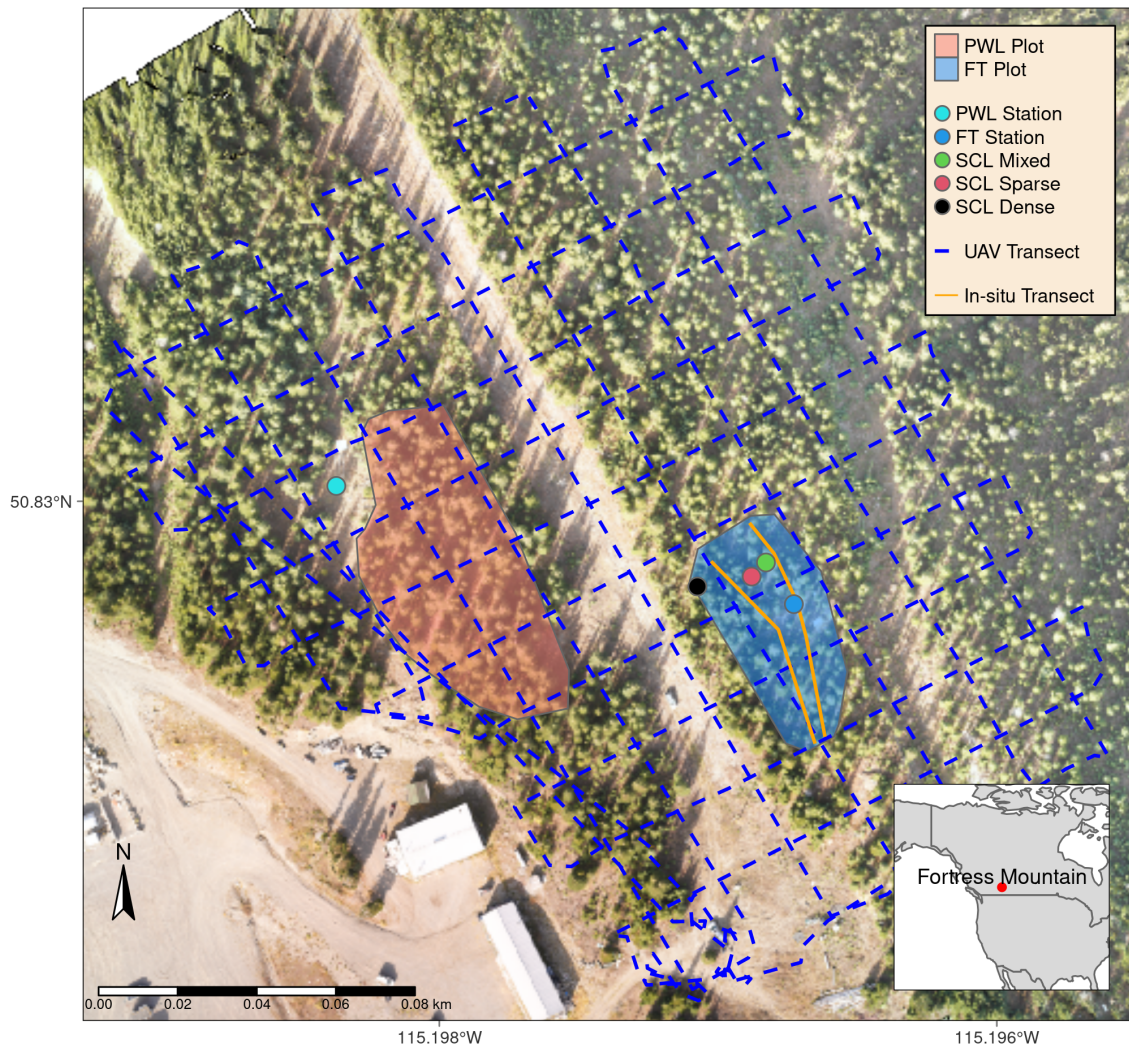


Figure 1: Map showing the location of forest plots, flux towers, subcanopy lysimeter instruments (SCL), and survey transects. The inset map on the lower right shows the regional location of Fortress Mountain Research basin.

136 used for gap filling wind speed. Additional wind speed measurements were collected by two 3D  
137 sonic anemometers (Campbell Scientific CSAT3) installed at 2 m (raised to 3 m February 2022)  
138 and 13.5 m above the ground at FT station. Average wind speeds at these four heights were  
139 found to follow a logarithmic relationship for periods where the instruments were known to be  
140 clean of snow. Thus, a wind profile was fitted to these measurements using the Prandtl-von  
141 Kármán log-linear relationship:

$$\bar{u} = \frac{u_*}{k} \ln\left(\frac{z - d_0}{z_0}\right) \quad (5)$$

142 where  $\bar{u}$  is average wind speed ( $\text{m s}^{-1}$ ) at height,  $z$  (m) above the ground,  $u_*$  is the friction  
143 velocity ( $\text{m s}^{-1}$ ),  $d_0$  is the displacement height (m),  $z_0$  is the roughness length of momentum  
144 (m), and  $k$  is the dimensionless von Kármán Constant (0.4).

145 To determine the displacement height and roughness length parameters the function “optim”  
146 from the stats R package (R Core Team, 2024) was used. The parameters found for the  
147 wind speed profile include a roughness length of 0.50 m and displacement height of 0.58 m.  
148 At PWL station, the snowfall rate was measured by an Alter-shielded OTT Pluvio weighing  
149 precipitation gauge 2.6 m above ground, corrected for undercatch following phase correction  
150 by Harder & Pomeroy (2013) and catch efficiency by Smith (2007). Wind speed for undercatch  
151 correction was measured by a 3-cup anemometer (Met One model 014A) at a height of 2.6 m at  
152 PWL station. An optical disdrometer (OTT Parsivel2) provided measurements of hydrometeor  
153 particle size and vertical velocity. All measurements were recorded at 15-min intervals using  
154 Campbell Scientific dataloggers, except the Parsivel2 which was recorded at 1-minute intervals  
155 by an onsite computer.

### 156 3.3 Lysimeter Measurements

157 Three subcanopy lysimeters (SCLs) were installed surrounding the FT Station (Figure 1) to  
158 provide 15-minute interval measurements of throughfall as in MacDonald (2010). Figure 2

shows the three SCLs which consisted of a plastic horse-watering trough with an opening of  
 0.9 m<sup>2</sup> and depth of 20 cm suspended from a load cell (Intertechnology 9363-D3-75-20T1)  
 attached to an aluminum pipe connected between two trees. For 26 distinct snowfall events,  
 where canopy snow ablation rates were deemed negligible, the throughfall rate,  $q_{tf}$ , was calcu-  
 lated by dividing the weight of snow in the SCL by the cross-sectional area of the SCL opening  
 and determining the rate of change at 15-minute intervals. Canopy snow load was estimated  
 at the same 15-minute intervals during these events using Equation 1 and incorporating mea-  
 surements of  $q_{tf}$  from the SCLs and  $q_{sf}$  from the PWL snowfall gauge. Interception efficiency  
 was also calculated for these intervals using Equation 2. Timelapse imagery, mass change on  
 a weighed tree lysimeter “hanging tree” (Pomeroy & Schmidt, 1993) and in-situ observations  
 were used to ensure the ablation of snow intercepted in the canopy was minimal over each inter-  
 val. Additionally, the  $q_{tf}$  measurements were filtered to include observations with a snowfall  
 rate  $> 0 \text{ kg m}^{-2} \text{ hr}^{-1}$ , throughfall rate  $> 0.05 \text{ kg m}^{-2} \text{ hr}^{-1}$  and a snowfall rate greater than the  
 subcanopy lysimeter throughfall rate to minimize observations with unloading. The weighed  
 tree lysimeter, a live subalpine fir (*Abies lasiocarpa*) tree suspended from a load cell (Artech  
 S-Type 20210-100) measured the weight of canopy snow load,  $L_{wt}$  (kg). The weight of snow  
 intercepted on the weighed tree was scaled to an areal estimate of canopy snow load ( $L$ , kg  
 m<sup>-2</sup>) using measurements of areal throughfall (kg m<sup>-2</sup>) from manual snow surveys and snow-  
 fall from the PWL Station snowfall gauge (see description of method in Pomeroy & Schmidt,  
 1993). The canopy structure surrounding three SCLs is shown in Figure 2 and was measured  
 using hemispherical photography (Nikon Coolpix 4500 and EC-F8 hemispherical lens) and the  
 hemispheR R package Chianucci & Macek (2023). The leaf area index and canopy coverage  
 from hemispherical photo analysis is shown in Table 1.

Table 1: Canopy structure of the three subcanopy lysimeters (SCL) located proximal to the FT Station. Leaf area index (LAI) and Canopy Coverage was measured using hemispherical photo analysis with the R package hemispheR.

Name	LAI (-)	Canopy Coverage (-)
Sparse	1.59	0.73

Table 1: Canopy structure of the three subcanopy lysimeters (SCL) located proximal to the FT Station. Leaf area index (LAI) and Canopy Coverage was measured using hemispherical photo analysis with the R package hemispheR.

Name	LAI (-)	Canopy Coverage (-)
Mixed	1.86	0.78
Closed	2.11	0.82

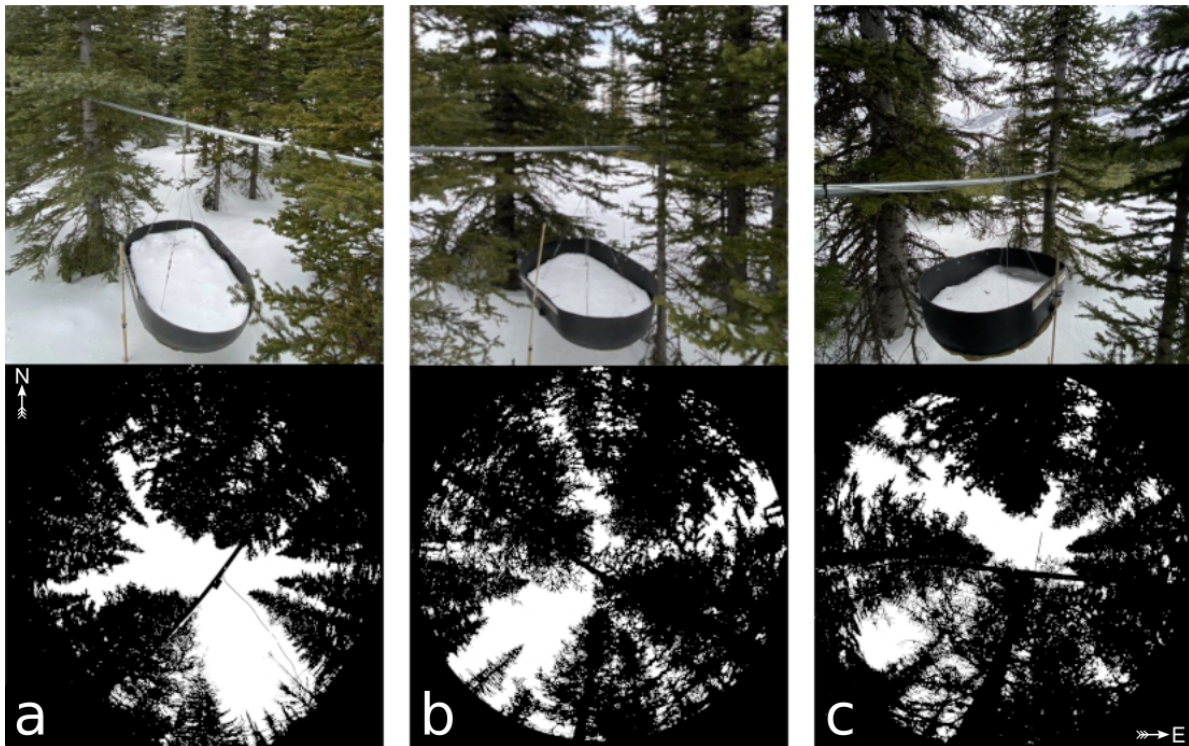


Figure 2: Images of the three subcanopy lysimeters (SCL) and surrounding canopy located in sparse (a), mixed (b), and dense (c) canopy. The top row presents a side view of each SCL and the bottom row shows hemispherical photographs classified using the hemispheR R package. These hemispherical images are oriented with north at the top and have been flipped to provide a view from above (i.e., east is on the right side of each image).

182 **3.4 UAV-Lidar Data Collection and Processing**

183 The UAV (FreeFly Alta X) payload included a REIGL miniVUX-2 airborne laser scanner,  
184 an Applanix APX-20 inertial measurement unit (IMU) and global navigation satellite system  
185 (GNSS). The UAV was flown 90 m above the ground at a speed of  $3 \text{ m s}^{-1}$  following the  
186 path shown in Figure 1. A detailed description of the UAV, payload, and flight settings is  
187 provided in the supporting information. The methods outlined by Harder et al. (2020) and  
188 Staines & Pomeroy (2023) were incorporated to reconcile survey lidar, IMU and GNSS data.  
189 A vertical offset of up to 6 cm between UAV-lidar flight lines was observed in the resulting  
190 point clouds on March 13<sup>th</sup> and 14<sup>th</sup>, 2024 and was attributed to IMU position drift. This  
191 offset between flight lines was corrected using the BayesStripAlign software v2.24 (BayesMap  
192 Solutions, 2024). After strip alignment, the mean elevation bias was 0.000 m and the RMS  
193 error declined from 0.055 m to 0.038 m on March 13<sup>th</sup> and changed from 0.033 m to 0.029  
194 m on March 14<sup>th</sup>. The point cloud density ranged from ~1200 returns  $\text{m}^2$  in sparse forest to  
195 ~2200 returns  $\text{m}^2$  in open clearings after flight paths were combined for each survey. Quality  
196 control, ground classification, calculation of the change in between two UAV-lidar point clouds,  
197 and raster generation (0.05 m grid cell resolution) was conducted using the LAStools software  
198 package (LAStools, 2024). Post processing and resampling of raster data to a 0.25 m grid cell  
199 resolution was conducted using the ‘Terra’ R package (Hijmans, 2024). More details on the  
200 UAV-lidar processing workflow are provided in the supporting information.

201 **3.5 Snow Surveys**

202 **3.5.1 In-situ Snow Depth and Density**

203 Twelve in-situ fresh snow surveys (six pre- and post-snowfall event pairs) provided measure-  
204 ments of subcanopy throughfall depth and density at 30 locations following the transects shown  
205 in Figure 1 to upscale the weighed tree snow load as in Hedstrom & Pomeroy (1998). Minimal  
206 ablation and redistribution of snow was observed between the pre- and post-snowfall surveys.

When conditions allowed for a UAV-lidar flight, the in-situ snow surveys were conducted following the UAV-lidar flight to assess the accuracy of the throughfall measurements and provide a fresh snow density for the calculation of SWE ( $\text{kg m}^{-2}$ ). A  $1000 \text{ cm}^3$  Perla snow density wedge sampler (RIP Cutter, <https://snowmetrics.com/shop/rip-1-cutter-1000-cc/>) was used to measure the density of the fresh snow layer,  $\overline{\rho_{tf}}$  ( $\text{kg m}^{-3}$ ) from snow pits. Throughfall depth measurements,  $\Delta HS$  were converted to SWE using the following equation:

$$\Delta SWE_{tf} = \Delta HS \cdot \overline{\rho_{tf}} \quad (6)$$

Differential GNSS rover coordinates, with  $\pm 2.5 \text{ cm}$  3D uncertainty, were taken at each snow sampling location so the locations could be queried later from the UAV-lidar rasters to assess measurement error and were also used as input for the UAV-lidar strip alignment. If a pre-event crust layer was present, the depth of post event fresh snow accumulation above the crust layer was interpreted as throughfall over the event. In the absence of a defined crust layer, the difference in pre- and post-event snow depth to ground was interpreted as event throughfall.

### 3.5.2 UAV-Lidar Snow Depth

Two uncrewed aerial vehicle (UAV) lidar surveys were conducted before and after a 24-hour snowfall event that occurred between March 13<sup>th</sup> and March 14<sup>th</sup>, 2023 to facilitate the measurement of snow accumulation and canopy structure within the FT and PWL forest plots. This period was selected based on two criteria: 1) it provided sufficient cumulative snowfall to result in a low relative error in UAV-LiDAR measured throughfall, and (2) minimal redistribution and ablation was observed, as confirmed by the SCLs, weighed tree, and time-lapse imagery. The change in elevation between the two UAV-lidar surveys was interpreted as the increase in snow accumulation,  $\Delta HS$  over the snowfall event.

228 **3.6 UAV-Lidar Canopy Metrics**

229 To characterize the canopy structure, the voxel ray sampling (VoxRS) methodology for lidar  
230 data analysis was employed, as developed by Staines & Pomeroy (2023), for the two UAV-  
231 lidar surveys. This method was chosen for its ability to provide canopy metrics that are less  
232 sensitive to the inherent non-uniform nature of lidar sampling data, which often results from  
233 beam occlusion in vegetation and leads to reduced points near the ground. Using this method  
234 radiation transmittance,  $\tau$  (-), was measured across the hemisphere at a  $1^\circ$  step, i.e., azimuth  
235 angles ( $0^\circ, 1^\circ, \dots, 359^\circ$ ) and zenith angles ( $0^\circ, 1^\circ, \dots, 90^\circ$ ) for each 0.25 m grid cell within the  
236 FT and PWL forest plots. The fraction of snow-leaf contact area per unit area of ground  
237 proposed by Hedstrom & Pomeroy (1998), and hereafter called leaf contact area ( $C_p$ ), was  
238 then calculated as:

$$C_p(C_c, \theta_h, L) = 1 - \tau \quad (7)$$

$$C_p(C_c, \theta_h, L) = \begin{cases} 1 - \tau, & \text{if } \theta_h > 0^\circ \\ 1 - \tau \approx C_c, & \theta_h = 0^\circ \end{cases} \quad (8)$$

239 where  $C_p$  is a function of the canopy coverage  $C_c$ ,  $\theta_h$  and  $L$ .  $C_p$  is approximately equal  
240 to canopy coverage ( $C_c$ ) for vertical snowfall trajectories. However, for non-vertical snowfall  
241  $1 > C_p > C_c$ .

242 **3.7 Statistics and Regression Models**

243 To determine how forest structure was associated with interception efficiency at different az-  
244 imuth and zenith angles over the March 13–14 snowfall event, the entire hemisphere at each  
245 grid location was considered. The relationship between interception efficiency and canopy  
246 contact number was found to be linear and thus the Pearson Correlation Coefficient,  $\rho_p$  was

calculated using the ‘stats’ package in R (R Core Team, 2024) to quantify the association between a single raster of interception efficiency and the 32,760 rasters containing the canopy contact number hemisphere for each portion of the hemisphere (azimuth [0°, 1°, ..., 359°], zenith angle [0°, 1°, ..., 90°]) for each of the 25 cm grid cells across the FT and PWL forest plots.

Linear and non-linear regression models were developed to assess relationships in the observed data. Linear models were fitted using ordinary least squares regression via the ‘lm’ function from the R ‘stats’ package (R Core Team, 2024) to analyze two relationships: (1) between interception efficiency and meteorological variables and (2) between interception efficiency and leaf contact area. The latter was forced through the origin based on the theoretical justification that the dependent variable should be zero when the independent variable is zero. Kozak & Kozak (1995) noted, the default  $R^2$  value provided for least squares models forced through the origin by many statistical packages can be misleading. Therefore, these  $R^2$  values were adjusted using Equation 10 in Kozak & Kozak (1995). Non-linear models were fitted using non-linear least squares regression via the ‘nls’ function in ‘stats’ package in R.

## 4 Results

### 4.1 The influence of meteorology on snow interception

Canopy snow load was estimated for 26 snowfall events and increased linearly with cumulative event snowfall without evidence of reaching a maximum (Figure 3). Over these events, air temperature ranged from -24.5°C to 1°C, wind speeds at 4.3 m height ranged from calm to  $4.6 \text{ m s}^{-1}$  (Table 2), and wind direction was predominately from the southwest during snowfall (Figure 4). Missing canopy snow load measurements in Figure 3 for certain troughs during specific events was caused by damage to the subcanopy lysimeter wiring due to animals and heavy snow loads.

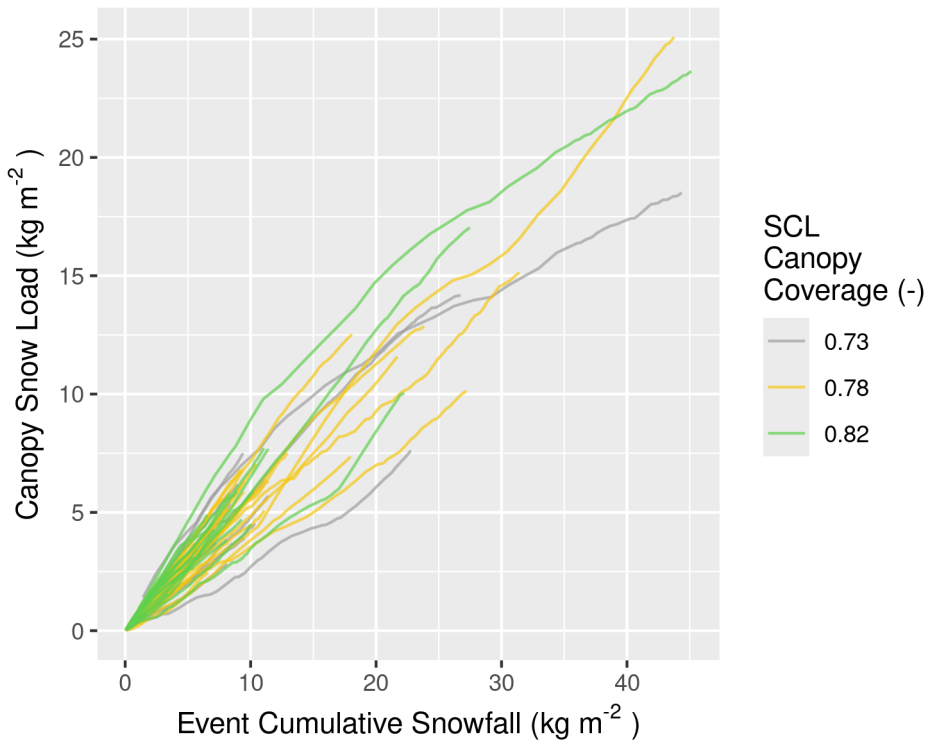


Figure 3: Plot showing the cumulative event snowfall versus the corresponding state of canopy snow load calculated using the SCLs for each of the 26 snowfall events. The SCLs are denoted by a distinct colour (grey, yellow, and green), correspond to varying canopy coverage (0.73, 0.78, and 0.82, respectively).

Table 2: Meteorology of the 26 snowfall events. Air temperature and wind speed were measured at FT station. Snowfall was measured at PWL station. Interception efficiency is estimated from snowfall and the average throughfall of all three SCLs located within the FT forest plot (all from 15-min. measurements).

Start Date	Air Temperature (°C)			Wind Speed (m/s)			Interception Efficiency (-)			Total Snowfall (mm)
	Min	Mean	Max	Min	Mean	Max	Min	Mean	Max	
2021-12-23	-6.2	-5.3	-4.6	0.6	3.1	4.6	0.7	0.8	1.0	21.7
2022-01-02	-15.9	-10.6	-5.8	0.2	1.9	4.2	0.1	0.7	1.0	32.9
2022-01-17	-14.8	-7.8	-0.8	0.2	1.1	1.8	0.0	0.6	1.0	12.9
2022-01-31	-24.5	-12.1	-6.4	0.1	1.0	1.7	0.2	0.7	1.0	9.1
2022-02-14	-9.9	-9.0	-8.5	0.4	0.8	1.2	0.2	0.5	0.8	1.7
2022-02-19	-4.7	-3.2	-2.5	1.3	2.3	3.6	0.3	0.6	0.9	11.1
2022-03-01	-8.3	-5.4	-1.0	0.1	1.0	3.1	0.4	0.8	1.0	9.9
2022-03-07	-12.5	-8.6	-4.4	0.3	0.8	1.7	0.3	0.7	1.0	9.5
2022-03-14	-2.7	-2.1	-0.8	1.0	1.6	2.9	0.2	0.6	0.9	8.4
2022-03-19	-3.1	-2.8	-2.5	0.0	0.7	1.3	0.3	0.5	0.6	6.6
2022-03-23	-7.9	-5.3	-0.9	0.8	1.2	1.8	0.4	0.6	0.9	1.6
2022-04-04	-3.5	-2.9	-2.1	0.6	1.0	1.9	0.0	0.4	0.6	3.4
2022-04-18	-5.2	-4.0	-2.7	0.4	1.1	1.9	0.1	0.5	0.9	7.4
2022-04-22	-2.8	-1.8	-0.5	0.4	0.8	1.2	0.1	0.5	1.0	9.8
2022-05-09	-4.9	-4.3	-3.2	0.1	0.4	0.9	0.2	0.5	0.9	8.1
2022-05-19	-4.9	-2.1	0.3	0.1	0.4	0.9	0.2	0.6	0.9	7.1
2022-06-13	-1.1	-0.3	0.6	0.1	0.1	0.4	0.0	0.5	0.9	45.3
2022-12-27	-3.0	-2.7	-1.9	0.6	1.1	1.8	0.2	0.5	0.9	4.5
2023-01-27	-11.5	-7.3	-4.5	0.6	0.9	1.2	0.1	0.5	0.8	10.4
2023-02-19	-14.3	-9.5	-6.3	0.2	0.8	1.4	0.2	0.7	1.0	18.1
2023-02-26	-9.2	-8.4	-6.6	0.2	1.0	2.1	0.3	0.5	1.0	5.4
2023-03-13	-8.9	-3.6	-0.1	0.3	1.3	2.2	0.0	0.5	1.0	27.4
2023-03-24	-7.9	-5.7	-3.5	0.1	0.5	1.2	0.1	0.4	0.7	23.8
2023-04-01	-8.9	-7.7	-4.7	0.1	0.6	1.4	0.4	0.6	0.8	11.4
2023-04-10	-1.1	-0.5	0.3	0.1	0.3	1.0	0.2	0.4	0.6	18.0
2023-05-08	0.2	0.6	1.0	0.4	0.6	0.8	0.6	0.6	0.7	3.5

271 Event average air temperature and interception efficiency were negatively associated for the

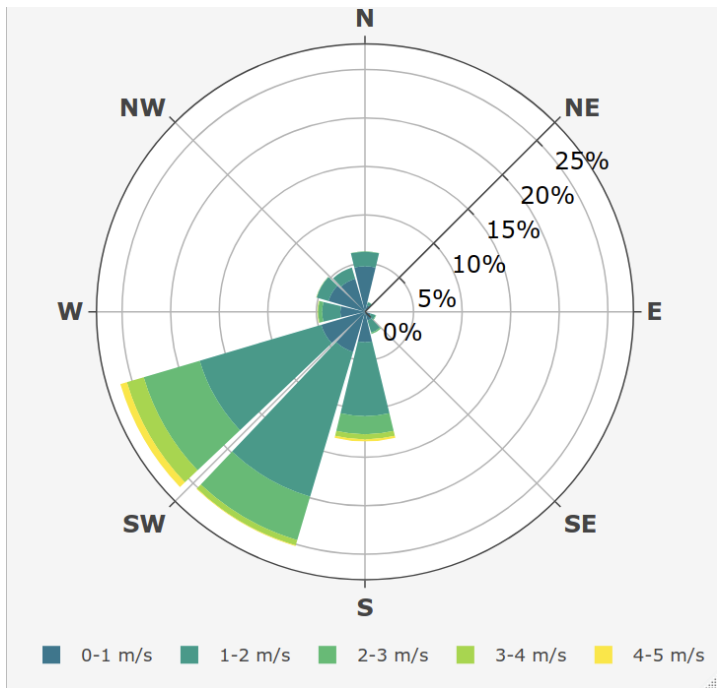


Figure 4: Wind rose showing the frequency of wind speed and direction over the 26 snowfall periods for the ultrasonic anemometer 4.3 m above ground at FT station.

mixed canopy ( $R^2 = 0.1$ ,  $p < 0.05$ ), but not associated at the closed and sparse canopies (Table 3 & Figure 5). Cumulative event snowfall was not associated with event interception efficiency at any site ( $p > 0.05$ ). Event wind speed was positively associated with interception efficiency for the sparse ( $R^2 = 0.1$ ,  $p > 0.05$ ) and closed ( $R^2 = 0.2$ ,  $p < 0.05$ ) canopies, both with limited canopy openings (Figure 2a,c) towards the prevailing wind direction (Figure 4). However, interception efficiency in the mixed canopy, which is open towards the prevailing wind direction, was not associated with wind speed ( $p > 0.05$ ).

Table 3: Statistics corresponding to the ordinary least squares linear regression test between independent variables: mean event air temperature, cumulative event snowfall, and mean event wind speed, and the dependent variable mean event interception efficiency. The test was run separately for three levels of canopy coverage ( $C_c$ ).

SCL					
Dependent Variable	Name	$C_c$	Adjusted $R^2$	p-value	$n$
Air Temperature (°C)	Sparse	0.73	-0.032	0.519	19
Air Temperature (°C)	Mixed	0.78	0.141	0.033	26
Air Temperature (°C)	Closed	0.82	0.008	0.297	20
Cumulative Snowfall (kg m <sup>-2</sup> )	Sparse	0.73	-0.038	0.568	19
Cumulative Snowfall (kg m <sup>-2</sup> )	Mixed	0.78	0.030	0.197	26
Cumulative Snowfall (kg m <sup>-2</sup> )	Closed	0.82	-0.049	0.732	20
Wind Speed (m/s)	Sparse	0.73	0.114	0.087	19
Wind Speed (m/s)	Mixed	0.78	0.010	0.275	26
Wind Speed (m/s)	Closed	0.82	0.192	0.030	20

Fifteen-minute interval measurements of interception efficiency and air temperature were not associated, despite significant relationships for the sparse and mixed canopies ( $R^2 < 0.03$ ,  $p < 0.05$ ), due to low predictive power (Figure 6a). The average interception efficiency across differing bins of air temperature also does not show any systematic trend (Figure 6a). However, a significantly greater median interception efficiency ( $p < 0.05$ ) was found for binned measure-

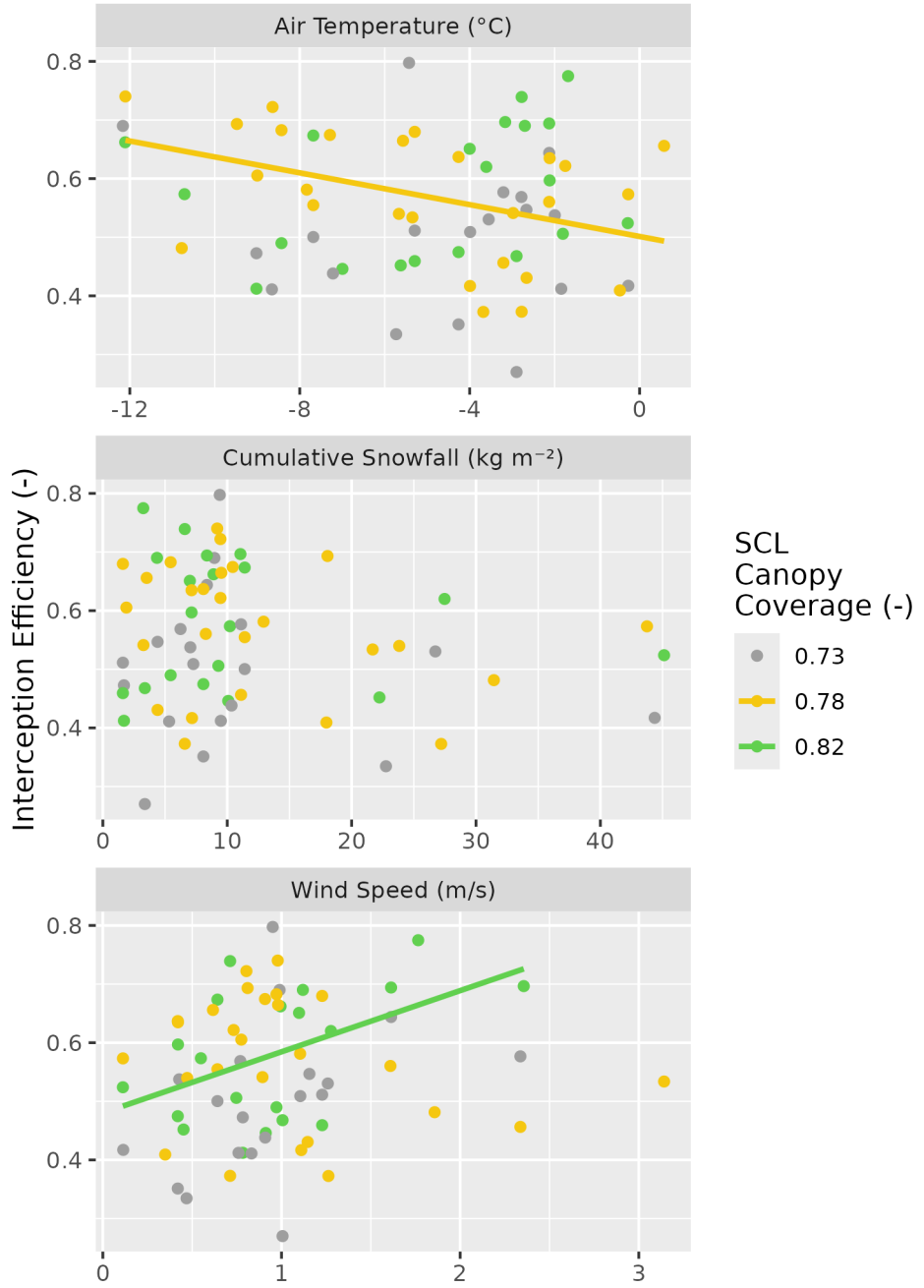


Figure 5: Scatter plots showing the event mean air temperature, mean wind speed, and cumulative snowfall versus the event mean interception efficiency estimated using the SCLs for each of the 26 snowfall events. The colours (grey, yellow, and green), correspond to varying canopy coverage (0.73, 0.78, and 0.82, respectively). A linear regression line fit to the data for significant relationships ( $p < 0.05$ ) is shown by the solid coloured lines. See Table 3 for linear regression statistics.

<sup>284</sup> ments with air temperatures below -6 °C compared to those with warmer air temperatures  
<sup>285</sup> using non-parametric Wilcoxon signed rank test.

<sup>286</sup> Mean wind speed was weakly associated with interception efficiency for the sparse ( $R^2 = 0.1$ ,  $p$   
<sup>287</sup>  $> 0.05$ ) and closed ( $R^2 = 0.2$ ,  $p < 0.05$ ), but not for the mixed canopy ( $p > 0.05$ ) (Table 4). The  
<sup>288</sup> binned data show an increasing trend in interception efficiency with increasing wind speed for  
<sup>289</sup> the sparse and closed canopies (Figure 6b). A comparison of interception efficiencies binned for  
<sup>290</sup> low ( $< 1 \text{ m s}^{-1}$ ) and high ( $> 1 \text{ m s}^{-1}$ ) wind speeds by the Wilcoxon signed rank test, showed that  
<sup>291</sup> high wind speeds had significantly higher ( $p < 0.05$ ) median interception efficiencies compared  
<sup>292</sup> to the low wind speed bins for the closed and sparse canopy. Conversely, the Wilcoxon test  
<sup>293</sup> showed the mixed canopy, which had an opening in the canopy towards the prevailing wind  
<sup>294</sup> direction (Figure 2b), had significantly higher ( $p < 0.05$ ) median interception efficiencies for  
<sup>295</sup> the low wind speed bins.

<sup>296</sup> Interception efficiency showed no association ( $R^2 < 0.05$ ,  $p > 0.2$ ) with the canopy load mea-  
<sup>297</sup> sured at the beginning of the 15-minute intervals (Table 4). The binned data show a small  
<sup>298</sup> increase in interception efficiency for all three canopies when the snow load is less than  $7 \text{ kg m}^{-2}$   
<sup>299</sup> (Figure 6c). Interception efficiency later declined for snow loads greater than  $7 \text{ kg m}^{-2}$  for all  
<sup>300</sup> canopies, though this was inconsistent for the mixed canopy. A significantly greater ( $p < 0.05$ )  
<sup>301</sup> median interception efficiency was found for canopy snow loads less than  $10 \text{ kg m}^{-2}$  than those  
<sup>302</sup> with high initial canopy snow loads ( $> 10 \text{ kg m}^{-2}$ ) using the Wilcoxon rank-test. Additional  
<sup>303</sup> statistics from ordinary least squares regression test on the 15-minute interval measurements  
<sup>304</sup> are provided in Table 4.

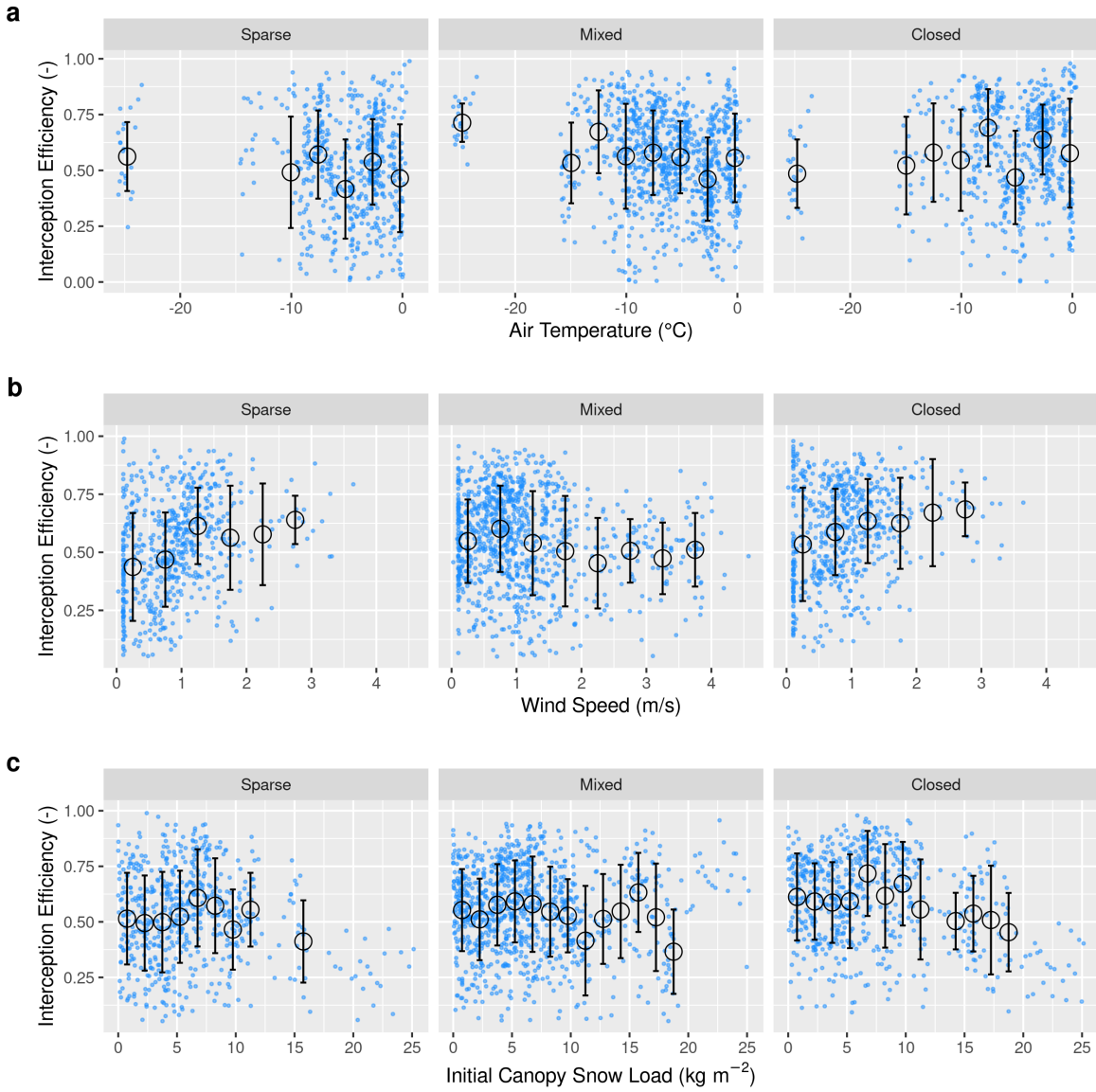


Figure 6: Scatter plots of 15-minute interval measurements (blue dots) and binned data (black open circles with error bars) of mean air temperature, mean wind speed, and initial canopy snow load versus mean snow interception efficiency. Panels show (a) air temperature, (b) wind speed, and (c) initial canopy snow load (the snow load observed at the beginning of the timestep). The black open circles show the mean of each bin and the error bars represent the standard deviations. See Table 4 for linear regression statistics.

Table 4: Statistics corresponding to the ordinary least squares linear regression test between 15-minute interval measurements of independent variables: mean air temperature, mean wind speed, and initial canopy snow load and the dependent variable mean interception efficiency. The test was run separately for three levels of canopy coverage ( $C_c$ ).

Dependent Variable		SCL	$C_c$	Adjusted $R^2$	p-value	n
Air Temperature (°C)	Mixed	0.78	0.032	0.000	985	
Air Temperature (°C)	Closed	0.82	0.004	0.069	618	
Air Temperature (°C)	Sparse	0.73	0.007	0.019	603	
Wind Speed (m/s)	Mixed	0.78	0.017	0.000	985	
Wind Speed (m/s)	Closed	0.82	0.037	0.000	618	
Wind Speed (m/s)	Sparse	0.73	0.089	0.000	603	
Initial Canopy Snow Load (kg m <sup>-2</sup> )	Mixed	0.78	0.000	0.453	972	
Initial Canopy Snow Load (kg m <sup>-2</sup> )	Closed	0.82	0.051	0.000	607	
Initial Canopy Snow Load (kg m <sup>-2</sup> )	Sparse	0.73	0.025	0.000	592	

## 4.2 The influence of forest structure on snow interception

UAV-lidar measurements of throughfall and canopy structure provide insights on how the forest canopy influenced subcanopy snow accumulation during a wind-driven snowfall event between March 13<sup>th</sup> and 14<sup>th</sup> 2023. This event totaled 28.7 kg m<sup>-2</sup> of snowfall at PWL station and was characterized by a transition from low rates of snowfall and air temperatures near 0°C to higher rates of snowfall by late afternoon on March 13<sup>th</sup> coinciding with air temperatures around -2.5 °C. An average wind speed of 1.3 m s<sup>-1</sup> and direction of 188° was observed 4.3 m above the ground at FT Station. Figure 7 shows Cionco's (1965) exponential function was not appropriate for this sparse canopy. The predicted hydrometeor trajectory angles at varying heights, calculated using Equation 4 and the mean observed hydrometeor terminal velocity observed over the event of 0.9 m s<sup>-1</sup> are also shown in Figure 7. An average wind speed of

<sup>316</sup> 1.6 m s<sup>-1</sup> and direction of 188° was calculated by integrating the wind speed from the surface  
<sup>317</sup> to the mean canopy height of FT plot. The corresponding trajectory angle calculated using  
<sup>318</sup> Equation 4 from this integrated wind speed was 61.5°.

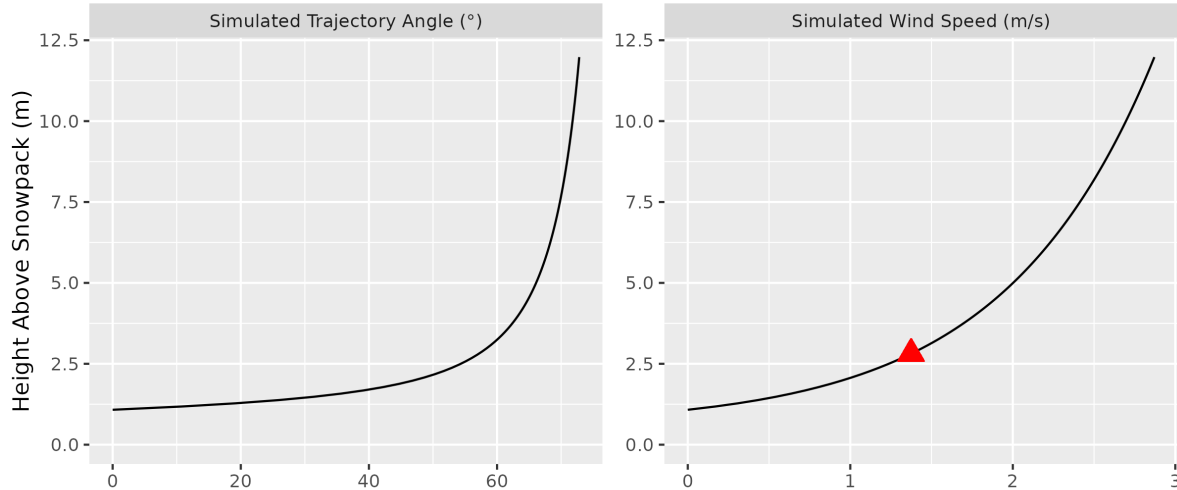


Figure 7: Wind speed profile using roughness length and displacement height parameters derived from anemometers at 2, 3, 4.3, and 13.5 m above ground at FT station over snow free periods and friction velocity estimated over the March 13–14<sup>th</sup> snowfall event. The red triangle shows the mean observed wind speed at 4.3 m height (2.8 m above the snowpack) measured at the FT station over the event.

<sup>319</sup> Throughfall depth measured by UAV-lidar was close to the 28 in-situ manual measurements  
<sup>320</sup> with a mean bias of -0.001 m and RMSE of 0.024 m. More details on the accuracy of UAV-lidar  
<sup>321</sup> snowdepth measurements are provided in the supporting information section. Figure 8 shows  
<sup>322</sup> the spatial distribution of throughfall and interception efficiency at the PWL and FT forest  
<sup>323</sup> plots. Reduced throughfall and greater interception efficiency was observed on the north (lee)  
<sup>324</sup> side of individual trees, which may be due to non-vertical hydrometeor trajectories caused by  
<sup>325</sup> the steady southerly winds observed over this event. Transparent areas within the forest plots  
<sup>326</sup> in Figure 8 represent grid cells that did not have any lidar ground returns (i.e., under dense  
<sup>327</sup> canopy proximal to tree trunks) or were masked due to disturbance (i.e., walking paths in  
<sup>328</sup> clearings). Visual observations on March 13<sup>th</sup> and 14<sup>th</sup> confirmed non-vertical hydrometeor  
<sup>329</sup> trajectories and increased canopy snow loads were observed on the windward side of individual

330 trees. This effect is shown in Figure 8 to be more apparent in the PWL forest plot than the  
331 FT forest plot. This may be attributed to the taller trees and higher canopy coverage of the  
332 PWL forest plot compared to the FT forest plot, as for the same trajectory angle a taller tree  
333 will produce a larger downwind footprint.

334 Figure 9 shows a strong linear correlation between  $C_p$  and interception efficiency towards the  
335 southern portion of the hemisphere, aligning with the average event wind direction. For the  
336 PWL forest plot, the upper 97.5<sup>th</sup> percentile of the  $\rho_p$  values shown in Figure 9, were found  
337 between azimuth angles of 167° – 217°. Similarly, for the FT forest plot, the upper 97.5<sup>th</sup>  
338 percentile of  $\rho_p$  was found between azimuth angles of 171°–223°. The zenith angle found  
339 to have the highest correlation over this azimuth range was 22° ( $\rho_p = 0.7$ ) and 21° ( $\rho_p =$   
340 0.83) for PWL and FT respectively. The high correlation coefficients found for non-vertical  
341 zenith angles for both PWL and FT are hypothesized to result from non-vertical hydrometeor  
342 trajectories.

343 The correlation between  $C_p$  and interception efficiency, resampled to a 5 m grid resolution, was  
344 higher when  $C_p$  was adjusted for the observed shift in hydrometeor trajectory (Vector Based),  
345 compared to the leaf contact angle measured at a zenith angle of 0° (nadir) (Figure 10). The  
346 the zenith angle observed to have the highest  $\rho_p$  in Figure 9 were used to adjust the vector  
347 based,  $C_p$  in Figure 10. The stronger association for the vector-based calculation suggests that  
348 adjusted  $C_p$  is a useful predictor of interception efficiency before ablation. An ordinary least  
349 squares linear regression forced through the origin was fit to the observed data points using  
350 the following equation:

$$\frac{I}{P} = C_p(C_c, \theta_h) \cdot \alpha \quad (9)$$

351 where  $\alpha$  is an efficiency constant which determines the fraction of snowflakes that contact the  
352  $C_p$  elements and are stored in the canopy (i.e., intercepted) before canopy snow unloading or  
353 ablation processes begin.

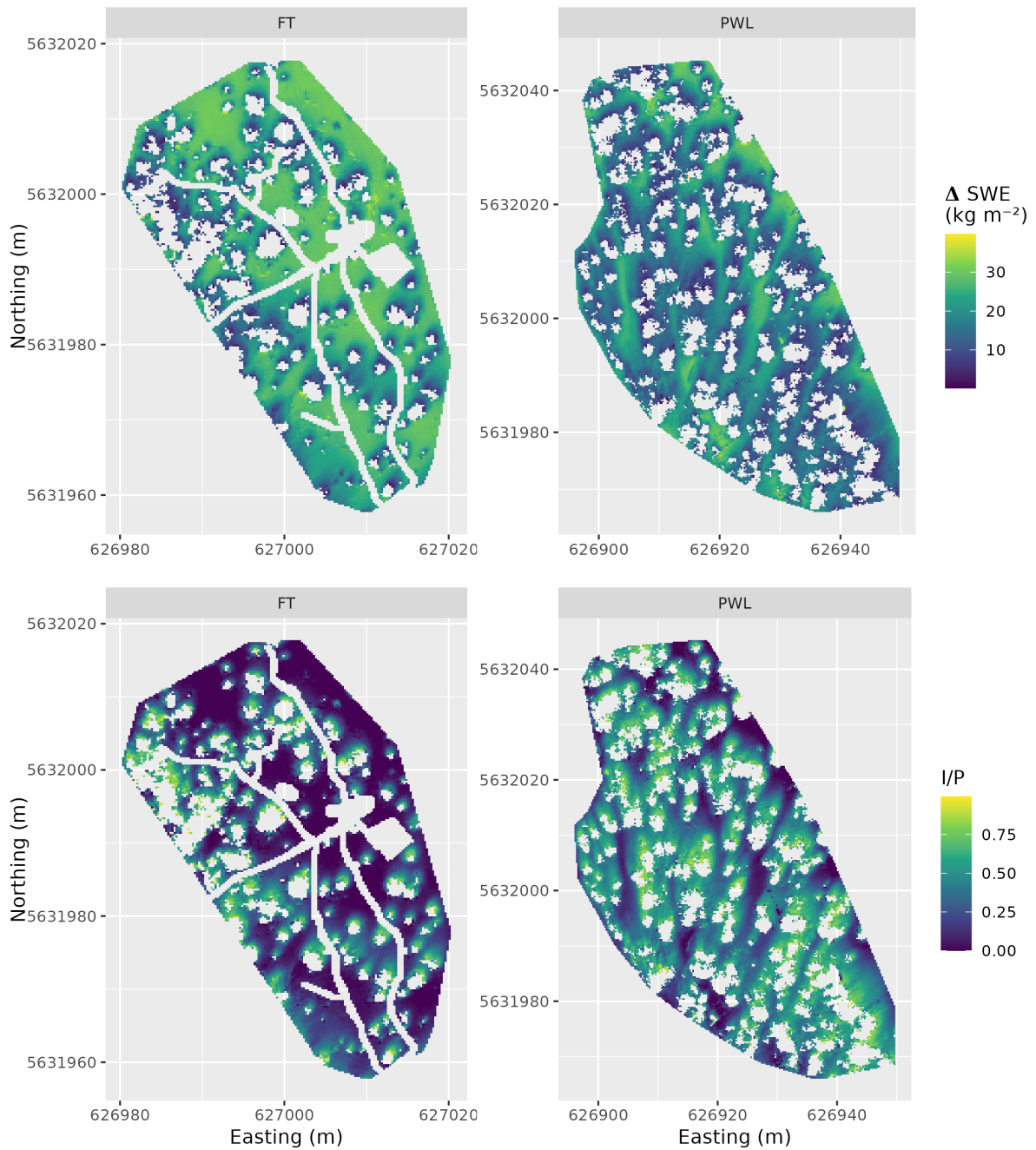


Figure 8: UAV-lidar measurements of the change in snow water equivalent, SWE ( $\text{kg m}^{-2}$ ) and interception efficiency, I/P (-), over the March 13, 2023 24-hour snowfall event for the FT and PWL forest plots at a 0.25 m resolution. See the location of the two forest plots in Figure 1.

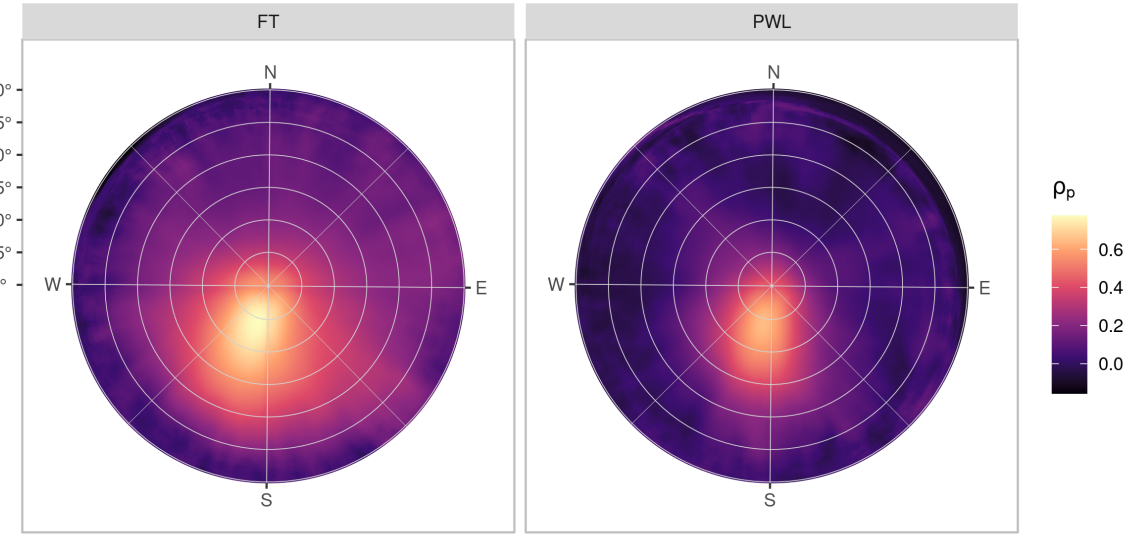


Figure 9: The Pearson Correlation Coefficient between rasters (25 cm resolution) of interception efficiency and leaf contact area for each grid cell across the study site for each azimuth angles ( $0^\circ, 1^\circ, \dots, 359^\circ$ ) and zenith angles ( $0^\circ, 1^\circ, \dots, 90^\circ$ ) for the FT (left) and PWL (right) forest plots.

For the vector-based model, the relationship between interception efficiency and  $C_p$  results in  $R^2$  values of 0.47 and 0.8 for PWL and FT respectively. The increase in interception efficiency with  $C_p$  follows a reduced slope compared to the nadir models with  $\alpha$  values of 0.71 and 0.68 for the PWL and FT plots respectively. The reduced slope for the vector-based models may be due to snowflakes that weaved through and/or bounced off branch elements in addition to UAV-lidar measurement uncertainty which may have been slightly affected by unloading and redistribution. These processes would have reduced the fraction of snowfall that was stored in the canopy. Model error statistics are presented in Table 5 for the nadir and vector-based models and show the vector-based model provided a better prediction of interception efficiency. Some of the scatter observed in the nadir model shown in Figure 10 may be explained by grid cells which observed a greater interception efficiency compared to the corresponding  $C_c$  value and can be attributed to the inability of  $C_c$  to represent the increase in interception observed within canopy gaps in Figure 8. Conversely, grid cells where interception efficiency is less than

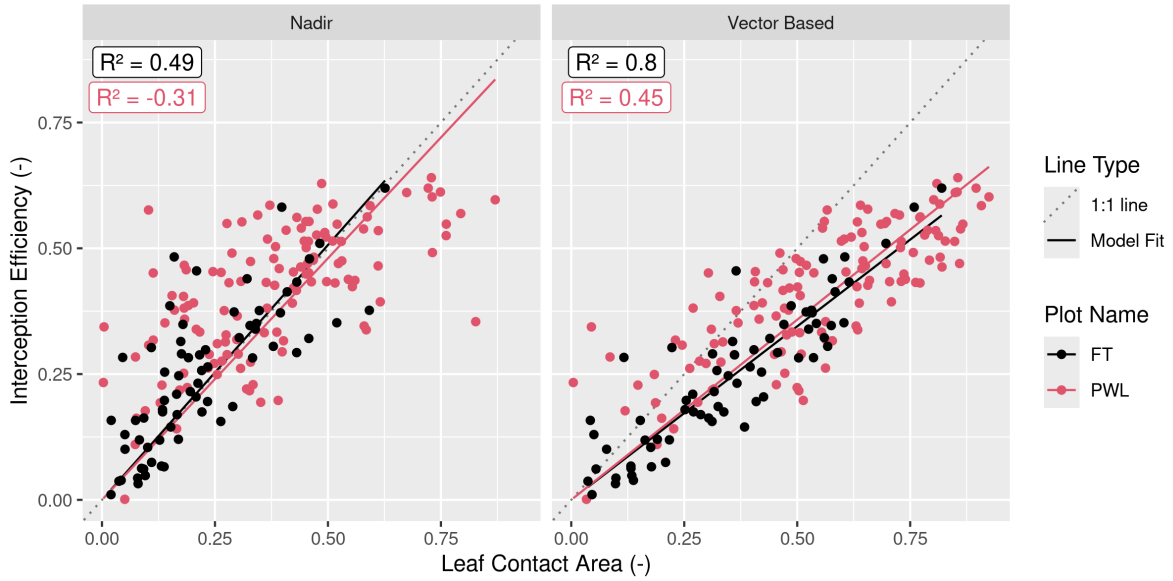


Figure 10: Scatter plots showing the relationship between leaf contact area and interception efficiency rasters resampled to a 5 m grid cell resolution. The left plot (nadir) shows leaf contact area measured from a zenith angle of  $0^\circ$ . The right plot (Vector Based) shows the leaf contact area averaged over rasters with zenith angles (PWL =  $22^\circ$ , FT =  $21^\circ$ ) and azimuth angles (PWL =  $167^\circ, 178^\circ, \dots 217^\circ$ ; FT =  $171^\circ, 172^\circ, \dots 223^\circ$ ). The solid lines (Model fit) show an ordinary least squares linear regression forced through the origin and fitted to the PWL (red) and FT (black) data and the light grey dotted line shows a 1:1 line. The  $R^2$  values for the four different models are shown in the upper right of each panel calculated following the methods outlined in Kozak & Kozak (1995).

367  $C_c$ , may be affected by non-vertical trajectory hydrometeors making their way underneath the  
368 canopy as observed by the reduced interception efficiency on the windward edges of individual  
369 trees in Figure 8. The latter explanation suggests the non-linear relationship observed for the  
370 PWL nadir calculation in Figure 8. The detailed point clouds required to derive the  $C_p$  values  
371 used in this analysis are rarely available and thus more accessible methods to estimate  $C_p$   
372 must be obtained to use Equation 9 which are described in the following section.

Table 5: Model error statistics provided for predictions of interception efficiency using Equation 9 and for different  $a$  values, as shown in the Model Slope column. Statistics are provided for the PWL and FT forest plots, using leaf contact area canopy metrics adjusted to zenith angles of ( $0^\circ, 1^\circ, \dots 30^\circ$ ) and azimuth angles ( $170^\circ, 171^\circ, \dots 220^\circ$ ) and nadir zenith angle of  $0^\circ$ . The Mean bias is the difference in the model and observed values, MAE is the mean of the absolute error, RMS Error is the root mean squared error,  $R^2$  is the coefficient of determination adjusted using Equation 10 in Kozak & Kozak (1995).

Plot	Canopy	Model Slope	Mean Bias	MAE	RMS Error	
Name	Calculation	(-)	(-)	(-)	(-)	$R^2$
FT	Nadir	0.99	0.022	0.071	0.099	0.51
FT	Vector Based	0.68	0.001	0.047	0.062	0.80
PWL	Nadir	0.95	0.048	0.113	0.146	NA
PWL	Vector Based	0.71	0.019	0.078	0.095	0.47

373 **4.3 The combined influence of trajectory angle and forest structure on**  
374 **interception**

375 Figure 11 shows that  $C_p$ , measured from VoxRS prior to snowfall on March 13<sup>th</sup>, increases  
376 substantially with simulated hydrometeor trajectory angle and corresponding simulated wind  
377 speed. The standard deviation in VoxRS measured  $C_p$ , illustrated by the shaded area in  
378 Figure 11, exhibits the broad range in values for individual grid cells across each forest plot.  
379 Despite this large scatter, a systematic increase in the mean  $C_p$  across both forest plots results  
380 from a rise in the number of canopy elements for more horizontal angles, when averaged across

381 each forest plot, over all azimuth angles (see top left panel Figure 11). This results in a large  
 382 rise in  $C_p$  over relatively common estimated wind speeds. For example, with a wind speed  
 383 of  $1 \text{ m s}^{-1}$  and estimated trajectory angle of  $48^\circ$ ,  $C_p$  would increase by 0.31 and 0.28 for the  
 384 PWL and FT forest plots respectively (Figure 11). This is a fractional increase in the plot  $C_p$   
 385 from nadir of 0.61 and 0.95 for PWL and FT respectively. The increase in  $C_p$  from  $C_c$ , with  
 386 increasing trajectory angle is shown on the bottom row of Figure 11 and exhibits a similar  
 387 relationship for both forest plots FT and PWL until trajectory angles reach approximately  
 388  $60^\circ$ . Beyond  $60^\circ$ , the PWL rate of increase slows as the  $C_p$  approaches 1.0, while the FT plot,  
 389 which has lower  $C_c$ , continues to rise until around  $75^\circ$  as a  $C_p$  of 1.0 is approached.  $C_p$  was  
 390 also quantified across trajectory angles for both PWL and FT on March 14<sup>th</sup>, post snowfall,  
 391 and showed a negligible increase in  $C_p$  compared to  $C_p$  measured on March 13<sup>th</sup> without snow  
 392 in the canopy.

393 A function is proposed here to calculate plot scale leaf contact area,  $C_p$  (-):

$$C_p = C_c + C_{inc}(\theta_h) \quad (10)$$

394 where,  $C_{inc}$  is the increase in leaf contact area from  $C_c$  which is a function of  $\theta_h$ . To estimate  
 395  $C_{inc}$  a non-linear least squares regression using a logistic function forced through the origin was  
 396 fit to the VoxRS measurements at FT and PWL for simulated hydrometeor trajectory angles  
 397 (see dashed lines in bottom row of Figure 11). A logistic function was selected to model this  
 398 relationship, as its shape reflects the slow increase in observed  $C_p$  at near vertical trajectory  
 399 angles, followed by a rapid increase to represent increase canopy area in the middle and lower  
 400 section of individual trees, and the gradual leveling off as  $C_p$  approaches a value of 1.0. The  
 401 logistic function used to predict  $C_{inc}$  as a function of  $\theta_h$  is:

$$C_{inc} = \left( \frac{C_{inc}^{max}}{1 + e^{\left( \frac{\theta_0 - \theta_h}{k} \right)}} - \frac{C_{inc}^{max}}{1 + e^{\left( \frac{\theta_0}{k} \right)}} \right) \quad (11)$$

402 where  $C_{inc}^{max}$  is the maximum value of  $C_{inc}$ ,  $\theta_0$  is the x-value of the sigmoid midpoint and  $k$  is

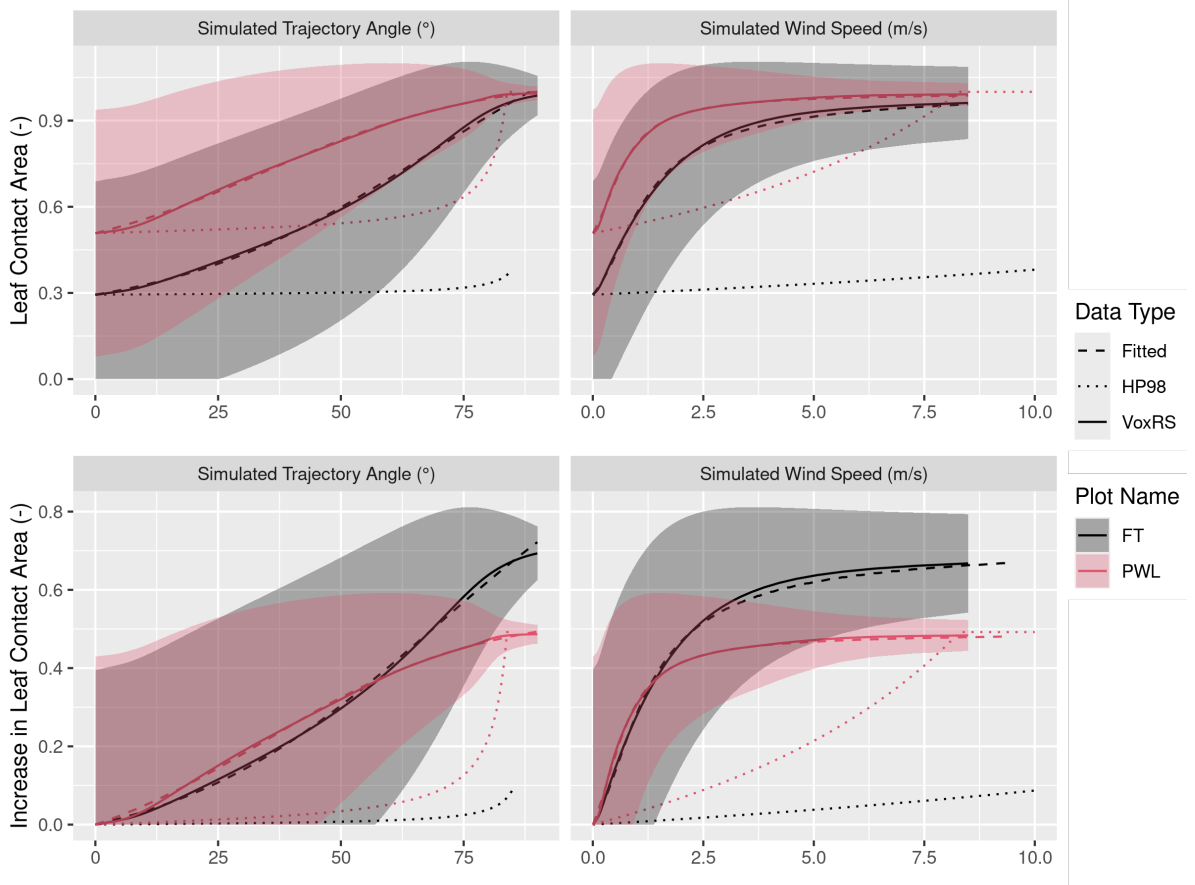


Figure 11: Plots showing the relationship between hydrometeor trajectory angle (left) and wind speed (right) with mean plot-wide snow-leaf contact area,  $C_p$  (top row) and the increase in mean plot-wide  $C_p$ , i.e.,  $C_p - C_c$  (bottom row). The hydrometeor trajectory angle is simulated through VoxRS and is measured as degrees from zenith. Simulated wind speed was calculated as a function of hydrometeor trajectory angle by rearranging Equation 4 and an observed event hydrometeor velocity of  $0.9 \text{ m s}^{-1}$ . The solid lines (VoxRS) represent the mean  $C_p$  (top row) or increase in mean  $C_p$  (bottom row) for a single zenith angle observed from VoxRS across all grid cells for each forest plot and across all azimuth angles. The shaded area represents 1 standard deviation above and below the observed VoxRS mean. The dashed lines (Fitted) represent predictions from Equation 10 (top) and Equation 11 (bottom). The dotted lines (HP98) represent the predictions from Equation 10 in Hedstrom & Pomeroy (1998). A forested downwind distance of 100 m was assumed for the HP98 calculation.

403 the logistic growth rate or steepness of the curve. The coefficients resulting from the non-linear  
 404 least squares regression fit of Equation 11 to the VoxRS dataset are presented in Table Table 6.  
 405 Simulated  $C_p$  using Equation 10 is shown in the dashed lines in the top row of Figure 11 and  
 406 follows closely to the VoxRS-measured mean  $C_p$ . Model error statistics shown in Table 7  
 407 demonstrate that Equation 11 performed well, with a mean bias and RMSE of 0.001 (-) and  
 408 0.0054 (-) respectively for PWL, and -0.0004 (-) and 0.0079 (-) for FT. In contrast, Table 7  
 409 reveals that the Hedstrom & Pomeroy (1998) method produced significantly less accurate  
 410 estimates of  $C_p$ , with a mean bias and RMSE of -0.201 (-) and 0.233 (-) respectively for PWL,  
 411 and -0.260 (-) and 0.324 (-) for FT.

Table 6: Coefficients derived from the non-linear least squares regression fit of Equation 11 to the VoxRS dataset.

Plot Names	$LCA_{max}$	$\theta_0$	$k$
PWL	0.66	34.58	22.14
FT	1.18	69.13	26.98

Table 7: Model error statistics calculated for the prediction of leaf contact area from trajectory angle using Equation 11 (nls) and Equation 10 from Hedstrom & Pomeroy (1998) for the PWL and FT forest plots. Mean bias is the difference in the model and observed values, MAE is the mean of the absolute error, RMS Error is the root mean squared error and  $R^2$  is the coefficient of determination. The units for all metrics are dimensionless. A forested downwind distance of 100 m was used for the HP98 calculation.

Model	Plot	Mean Bias (-)	MAE (-)	RMS Error (-)	$R^2$
HP98	FT	-0.2598	0.2598	0.3240	0.7196
HP98	PWL	-0.2008	0.2010	0.2326	0.4446
nls	FT	-0.0004	0.0067	0.0079	0.9987
nls	PWL	0.0010	0.0040	0.0054	0.9990

<sup>412</sup> **4.4 Throughfall Model Performance**

<sup>413</sup> The performance of Equations 9, 10, and 11 in estimating event throughfall was assessed  
<sup>414</sup> against UAV-lidar measurements of throughfall for the March 13–14<sup>th</sup> snowfall event at the  
<sup>415</sup> plot scale for both FT and PWL. Required values for the model included the event mean  
<sup>416</sup> hydrometeor terminal velocity and total event snowfall which were measured at PWL station,  
<sup>417</sup> and wind speed was taken as one-third the mean canopy height using the wind speed profile in  
<sup>418</sup> Figure 7. Additional model inputs include the mean  $C_c$  for each plot which was measured from  
<sup>419</sup> the VoxRS dataset. An  $\alpha$  value of 0.836 (-) was found through calibration which provided the  
<sup>420</sup> best fit between observed and simulated interception efficiency at the plot scale for both FT  
<sup>421</sup> and PWL.

<sup>422</sup> Figure 12 shows the vector-based model, computed using Equation 9 with  $C_p$  adjusted for  
<sup>423</sup> estimated hydrometeor trajectory angle, closely matches UAV-lidar measurements of through-  
<sup>424</sup> fall. Observed and modelled values of interception efficiency and  $\Delta SWE_{tf}$  are presented in  
<sup>425</sup> Table 8 along with corresponding error statistics. Modelled throughfall from the vector-based  
<sup>426</sup> model was 17 kg m<sup>-2</sup> compared to the measured throughfall of 16.6 kg m<sup>-2</sup> for PWL. For FT,  
<sup>427</sup> the modelled throughfall was 21.8 kg m<sup>-2</sup>, while the measured values were 22.1 kg m<sup>-2</sup>. The  
<sup>428</sup> vector-based model shows a lower mean bias of -0.3 kg m<sup>-2</sup> for PWL and a negative bias of  
<sup>429</sup> 0.3 kg m<sup>-2</sup> for FT, compared to the larger mean bias of -1.6 kg m<sup>-2</sup> for PWL and -0.8 kg m<sup>-2</sup>  
<sup>430</sup> for FT with the nadir-model (calculated using  $C_c$  in place of  $C_p$ ). This resulted in a large  
<sup>431</sup> reduction in the percent error in predicted throughfall, from -9.4% with the nadir-model to  
<sup>432</sup> -1.8% with the vector-based model for PWL. A smaller improvement was observed for FT,  
<sup>433</sup> with the percent error in predicted throughfall declining from -3.6% with the nadir-model to  
<sup>434</sup> -1.4% with the vector-based model.

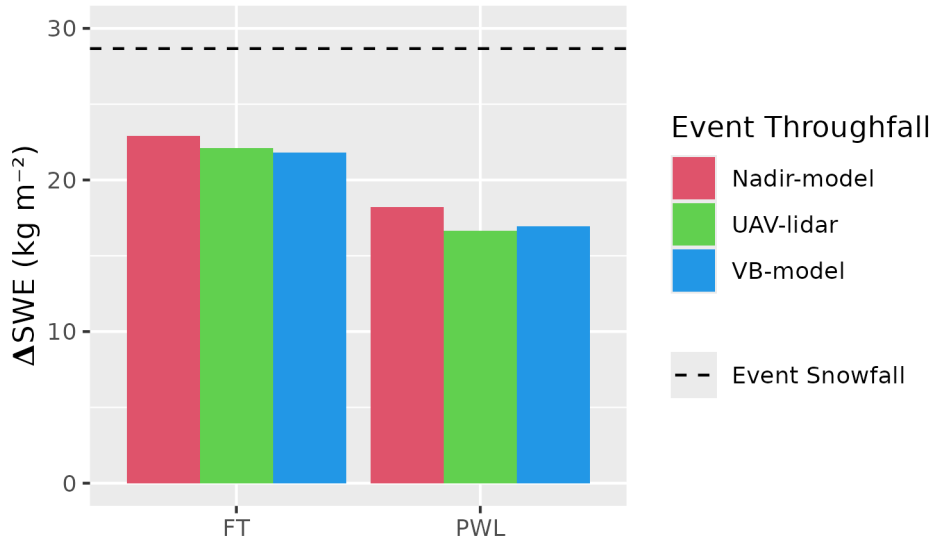


Figure 12: Bar chart comparing the observed and modelled mean change in throughfall (SWE,  $\text{kg m}^{-2}$ ) over the March 13-14 snowfall event averaged over forest plots FT and PWL. The ‘Nadir-model’ used Equation 9 not adjusted for trajectory angle (i.e.,  $C_c$ ) and the Vector-based ‘VB-model’ which uses Equation 9 with  $C_p$  adjusted for trajectory angle. ‘UAV-lidar’ corresponds to throughfall calculated using Equation 6 incorporating UAV-lidar snow depth and snow density from in-situ snow pits. The black horizontal dashed line shows the accumulated SWE ( $\text{kg m}^{-2}$ ) over the snowfall event to the PWL station open clearing.

Table 8: Model error statistics for model estimates of snow interception efficiency (I/P) and throughfall (TF) compared to measurements of I/P and TF using UAV-lidar averaged over the FT and PWL forest plots. Units for I/P are (-) and TF are ( $\text{kg m}^{-2}$ ). The vector-based model utilized Equation 9 with  $C_p$  adjusted for trajectory angle. The nadir model also utilized Equation 9 but was not adjusted for trajectory angle and thus  $C_c$  was used instead of  $C_p$ . The ‘Obs. Value’ column contains measurements from UAV-lidar while the ‘Mod. Value’ column contains the modelled values. The mean bias was calculated as observed minus modelled and percent error is the percent error between predicted and observed values.

Plot	Type	Model	Value	Units	Obs.	Mod.	Mean	
		Name			Value	Value	Bias	Perc. Error
FT	VB-model	I/P	-		0.23	0.24	-0.01	-4.67
FT	Nadir-model	I/P	-		0.23	0.20	0.03	12.10
FT	VB-model	TF	$\text{kg m}^{-2}$		22.12	21.82	0.31	1.38
FT	Nadir-model	TF	$\text{kg m}^{-2}$		22.12	22.91	-0.79	-3.58
PWL	VB-model	I/P	-		0.42	0.41	0.01	2.54
PWL	Nadir-model	I/P	-		0.42	0.37	0.05	12.95
PWL	VB-model	TF	$\text{kg m}^{-2}$		16.64	16.95	-0.31	-1.84
PWL	Nadir-model	TF	$\text{kg m}^{-2}$		16.64	18.20	-1.56	-9.35

## 435 5 Discussion

436 The point scale observations presented in Figure 6 show air temperature had little influence  
 437 on interception efficiency. This differs from existing studies which suggested either a positive  
 438 (Storck et al., 2002) or negative (Hedstrom & Pomeroy, 1998) relationship. A weak relation-  
 439 ship, that leaves 80–90% of variance unexplained, was observed between initial interception

<sup>440</sup> efficiency (before unloading) with increasing wind speed at two locations which were sheltered  
<sup>441</sup> from the predominant wind direction (Figure 6b). This is attributed to an associated increase  
<sup>442</sup> in  $C_p$  due to non-vertical hydrometeor trajectories. These results are consistent with observa-  
<sup>443</sup> tions by Schmidt & Troendle (1989) who observed a slight increase in snowfall interception  
<sup>444</sup> with increasing wind speeds up to  $6 \text{ m s}^{-1}$  and studies of rainfall interception by Herwitz &  
<sup>445</sup> Slye (1995) and Van Stan et al. (2011).

<sup>446</sup> Compared to the influence of wind speed, interception efficiency showed a smaller sensitivity  
<sup>447</sup> to canopy snow load at the point scale (Figure 5). The slight increase in interception efficiency  
<sup>448</sup> for smaller canopy snow loads and decline for larger canopy snow loads is attributed to the  
<sup>449</sup> influence of canopy snow load on  $C_p$  (Figure 6c). While small, this effect is consistent with  
<sup>450</sup> the theory proposed by Satterlund & Haupt (1967) that interception efficiency increases as  
<sup>451</sup> the canopy fills with snow bridging gaps in the canopy increasing, while later declining due to  
<sup>452</sup> branch bending and decreased canopy coverage. However, the observations shown in Figure 6  
<sup>453</sup> and Figure 3, which minimized ablation processes, differ from those reported by Satterlund  
<sup>454</sup> & Haupt (1967), Schmidt & Pomeroy (1990), and Moeser et al. (2015), as canopy snow load  
<sup>455</sup> increased linearly with snowfalls up to  $45 \text{ kg m}^{-2}$  without approaching a maximum canopy snow  
<sup>456</sup> load. The strong exponential decline in interception efficiency with increasing event snowfall  
<sup>457</sup> in these studies Schmidt & Pomeroy (1990) may have resulted from higher unloading rates as  
<sup>458</sup> branches bent under heavy snow loads, hence mixing ablation and interception processes to  
<sup>459</sup> varying degrees. In contrast, other studies (Calder, 1990; Watanabe & Ozeki, 1964) align with  
<sup>460</sup> the observations in Figure 6 and Figure 3, showing little evidence of a reduced interception  
<sup>461</sup> efficiency with increasing snowfall. The low sensitivity of interception efficiency with canopy  
<sup>462</sup> snow load found in this study and others may be attributed to several factors: a reduced  
<sup>463</sup> inclusion of ablation processes in the interception efficiency measurements, limited influence  
<sup>464</sup> of canopy snow load on  $C_p$  at this study site, and/or the compensatory effects outlined by  
<sup>465</sup> Satterlund & Haupt (1967).

<sup>466</sup> Staines & Pomeroy (2023) showed a slight increase in VoxRS  $C_p$  between snow-off and snow-on  
<sup>467</sup> conditions. However, the increase in  $C_p$  resulting from snow load in Staines & Pomeroy (2023)

468 was small compared to the substantial rise in  $C_p$  due to trajectory angle presented in their  
469 study and as shown in Figure 11. Both findings from Staines & Pomeroy (2023) corroborate  
470 the results reported in this study. Further evidence in support of the relatively small influence  
471 of canopy snow load on  $C_p$ , is provided by Lundquist et al. (2021) who reported improved  
472 simulation of subcanopy snow accumulation without the use of a maximum canopy snow load,  
473 when linked with a comprehensive canopy snow ablation routine. Lehtonen et al. (2016)  
474 also note that in northern Finland heavy canopy snow loads have been observed to continue  
475 increasing until stem breakage, under conditions favourable for the formation of significant  
476 rime-ice accretion and limited ablation, thus reducing  $C_p$ . Models are available to predict the  
477 accretion of ice on tree canopies (e.g., Nock et al., 2016) however, further research is required  
478 to understand the canopy snow load required to cause stem breakage across different tree  
479 species and canopy loads.

480 These findings on the limited influence of air temperature and canopy snow load on initial  
481 interception challenge the theoretical basis of many existing snow interception parameteriza-  
482 tions (Hedstrom & Pomeroy, 1998; Moeser et al., 2015; Satterlund & Haupt, 1967; Storck et  
483 al., 2002). To address this a new snow interception parameterization, Equation 9, is presented  
484 which calculates interception efficiency as a function of  $C_p$  and  $\alpha$ . This new parameterization  
485 allows for canopy snow loading processes to be isolated from canopy snow ablation processes  
486 and is consistent with current rainfall interception theory (Valante et al., 1997). Equation 9  
487 differs only slightly from the original Hedstrom & Pomeroy (1998) parameterization (see Equa-  
488 tion 6 in Hedstrom & Pomeroy (1998)), in that it does not calculate interception efficiency  
489 as a function of canopy snow load and from the Storck et al. (2002) parameterization who  
490 proposed interception efficiency to be constant over time and space. The theoretical basis of  
491 the  $\alpha$  parameter in Equation 9 is that the association between  $C_p$  and interception efficiency,  
492 as shown in Figure 10, unlike existing rainfall parameterizations (Valante et al., 1997) does not  
493 follow a 1:1 line, as falling snow hydrometeors may bounce off the canopy elements. Further  
494 research is needed to explore how processes such as the increased cohesion and adhesion of  
495 snowfall to the canopy at warm temperatures, as observed by Kobayashi (1987), Pfister &

<sup>496</sup> Schneebeli (1999), Storck et al. (2002), as well as hydrometeor velocity, particle size, and  
<sup>497</sup> shape suggested by (Katsushima et al., 2023), may influence the  $\alpha$  parameter, although these  
<sup>498</sup> effects were not observed in this study.

<sup>499</sup> Measurements of interception efficiency and canopy structure, as shown in Figure 8, align with  
<sup>500</sup> the theory proposed by Hedstrom & Pomeroy (1998) which suggests reduced throughfall on  
<sup>501</sup> the lee side of individual trees. However, an existing method proposed in Hedstrom & Pomeroy  
<sup>502</sup> (1998) to scale canopy coverage with wind speed failed to reproduce the observations presented  
<sup>503</sup> in Figure 11. A new method is proposed which uses a logistic function to calculate plot-wide  
<sup>504</sup>  $C_{inc}$  as a function of  $\theta_h$  and  $C_c$ . Significant scatter in VoxRS measured  $C_p$  across the two  
<sup>505</sup> forest plots, illustrated by the high standard deviation in Figure 11, resulted from directional  
<sup>506</sup> (azimuth) and spatial differences in canopy structure. This large scatter suggests the observed  
<sup>507</sup> relationships in Figure 11 are only applicable at the forest stand scale where the sub-metre  
<sup>508</sup> variability in  $C_p$  averages out. At the point scale, the mixed canopy SCL which is open to the  
<sup>509</sup> prevailing wind direction (Figure 2), and did not follow this relationship and led to an increase  
<sup>510</sup> in throughfall with increasing wind speed (Figure 5 & Figure 6). However, Figure 11 shows  
<sup>511</sup> that at the plot scale,  $C_p$  rises with increasing  $\theta_h$ , as there is a greater number of grid cells  
<sup>512</sup> which have more closed canopy at more horizontal angles. Thus at the plot scale, Equation 11,  
<sup>513</sup> which uses trajectory angle alone, was shown to successfully determine  $C_{inc}$  and thus  $C_p$  for  
<sup>514</sup> the discontinuous canopies of both the FT and PWL forest plots. However, Equation 11 would  
<sup>515</sup> not be applicable to areas that have large continuous gap fractions (e.g., large forested clear  
<sup>516</sup> cuts) that are many times wider than the mean canopy height. Further work is required to  
<sup>517</sup> refine the relationship proposed in Equation 11 across a range of tree species and densities.  
<sup>518</sup> Backflows and large eddies that occur within the canopy may also contribute to very mixed  
<sup>519</sup> responses (Staines & Pomeroy, 2023).

<sup>520</sup> It was found that the mean hydrometeor trajectory angle over a snowfall event, required for  
<sup>521</sup> Equation 11, could be predicted by using the observed hydrometeor fall velocity and a mean  
<sup>522</sup> horizontal wind speed selected at one-third of the canopy height above the ground. A wind  
<sup>523</sup> speed at one-third the mean canopy height is hypothesized to be important for canopy snow

524 accumulation as a large fraction of the horizontal cross-sectional area is at this height for most  
525 needleleaf canopies. Katsushima et al. (2023), also proposed the wind speed at one-third the  
526 canopy height for modelling unloading of canopy snow as it corresponds to the centre of gravity  
527 when the horizontal projection of the canopy is assumed to be a triangle. However, there is  
528 uncertainty in the transferability of the canopy height observed here to other environments  
529 due to differing tree structures and tree species. This may include forests with a larger trunk  
530 space or have more of their canopy contact area at higher heights above the ground (i.e., some  
531 deciduous canopies). Moreover, Equation 4 assumes a linear hydrometeor trajectory, and does  
532 not consider non-linear patterns such as wind flow directions around tree elements, turbulent  
533 flow, or differences in wind speed with height.

534 Although the improvement in performance of the vector-based model over the nadir model was  
535 relatively small, the vector-based model is preferred due to its overall lower error compared  
536 to the UAV-lidar measurements and better representation of physical processes. While the  
537 vector-based model acts to increase interception efficiency with wind speed, several studies  
538 have shown that canopy snow ablation increases as a result of wind induced unloading (Bartlett  
539 & Verseghy, 2015; Betts & Ball, 1997; Lumbrazo et al., 2022; Roesch et al., 2001; Wheeler,  
540 1987). Thus, representing both the increase in initial interception due to inclined hydrometeor  
541 trajectory angles and the subsequent increase in canopy snow unloading will be important in  
542 subcanopy snow accumulation models.

## 543 6 Conclusions

544 New observations of initial snow interception, collected over a wide range of meteorological  
545 conditions and canopy structures suggest forest structure is the primary factor governing  
546 subcanopy snow accumulation. At the point scale, high-temporal resolution measurements  
547 revealed no evidence of a maximum canopy snow load, even for event snowfalls up to 45 kg  
548 m<sup>-2</sup>, nor was there any indication of air temperature influencing the cohesion and adhesion of  
549 snowfall to the canopy or branch bending reducing canopy coverage. Instead, wind speed was

550 found to influence interception efficiency by changing the hydrometeor trajectory angle, which  
551 can lead to a substantial increase in snow-leaf contact area.

552 At the forest plot scale, UAV-lidar measurements of throughfall collected over a wind-driven  
553 snowfall event confirmed the results observed at the point-scale and showed leaf contact area  
554 was the main factor governing the interception efficiency at a particular site. The leaf contact  
555 area, which accounts for the change in canopy structure with trajectory angle, proved to be  
556 a better predictor of interception efficiency compared to nadir-calculated canopy coverage.  
557 When averaged across each forest plot, leaf contact area was shown to be highly sensitive to  
558 hydrometeor trajectory angle, increasing by 61–95% for trajectory angles associated with a  
559 1 m s<sup>-1</sup> wind speed. An existing theoretical relationship failed to adequately represent the  
560 VoxRS-measured increase in leaf contact area with simulated trajectory angles. As a result, a  
561 new relationship is proposed, which demonstrated good performance at this study site.

562 The weak association between air temperature and canopy snow load with interception effi-  
563 ciency, as presented here and in other recent studies, coupled with the considerable influence  
564 of wind speed on leaf contact area, highlights the need for a new snow interception parameter-  
565 ization. A new parameterization is proposed that calculates initial interception as a function  
566 of snowfall and leaf contact area. This parameterization is consistent with many rainfall in-  
567 terception studies, which also separate canopy loading and ablation processes, and calculate  
568 interception as a function of canopy coverage. Additionally, a second equation is proposed  
569 to estimate leaf contact area as a function of hydrometeor trajectory angle and nadir canopy  
570 coverage. This updated snow interception parameterization showed good performance in the  
571 subalpine forest in this study, but further validation should be conducted in a range of climates,  
572 forest species, and canopy structures.

## 573 7 Acknowledgments

574 We wish to acknowledge financial support from the University of Saskatchewan Dean's Schol-  
575 arship, Natural Sciences and Engineering Research Council of Canada, Global Water Futures

576 Programme, Environment and Climate Change Canada, Alberta Innovates, Canada Founda-  
577 tion for Innovation, and the Canada Research Chairs Programme. We thank Madison Harasyn,  
578 Hannah Koslowsky, Kieran Lehan, Lindsey Langs and Fortress Mountain Resort for their help  
579 in the field. Madison Harasyn, Alistair Wallace, and Rob White contributed to developing the  
580 UAV-lidar processing workflow.

## 581 **8 Data Availability**

582 The data that support the findings in this study are available at <https://github.com/acebulsk/snow->  
583 int-paper.

584 **9 References**

- 585 Axelsson, P. (2000). Peter Axelsson 110. *International Archives of Photogrammetry and*  
586 *Remote Sensing*, 33(4), 110–117. [https://www.isprs.org/proceedings/XXXIII/congress/part4/111\\_XXXIII-part4.pdf](https://www.isprs.org/proceedings/XXXIII/congress/part4/111_XXXIII-part4.pdf)
- 588 Bartlett, P. A., & Verseghy, D. L. (2015). Modified treatment of intercepted snow improves  
589 the simulated forest albedo in the Canadian Land Surface Scheme. *Hydrological Processes*,  
590 29(14), 3208–3226. <https://doi.org/10.1002/HYP.10431>
- 591 BayesMap Solutions. (2024). *BayesStripAlign*. <https://bayesmap.com/products/bayesstripalign/>
- 593 Betts, A. K., & Ball, J. H. (1997). Albedo over the boreal forest. *Journal of Geophysical*  
594 *Research: Atmospheres*, 102(D24), 28901–28909. <https://doi.org/https://doi.org/10.1029/96JD03876>
- 596 Calder, I. R. (1990). *Evaporation in the uplands* (p. 148). Wiley.
- 597 Chianucci, F., & Macek, M. (2023). hemispheR: an R package for fisheye canopy image  
598 analysis. *Agricultural and Forest Meteorology*. <https://doi.org/10.1016/j.agrformet.2023.109470>
- 600 Cionco, R. M. (1965). A Mathematical Model for Air Flow in a Vegetative Canopy. *Journal of*  
601 *Applied Meteorology* (1962), 4(4), 517–522. [https://doi.org/https://doi.org/10.1175/1520-0450\(1965\)004%3C0517:AMMFAF%3E2.0.CO;2](https://doi.org/https://doi.org/10.1175/1520-0450(1965)004%3C0517:AMMFAF%3E2.0.CO;2)
- 603 Clark, M. P., Wood, A., Nijssen, B., Bennett, A., Knoben, W., & Lumbrazo, C. (2020).  
604 *SUMMA v3.0.3*. Zenodo. <https://doi.org/10.5281/zenodo.4558054>
- 605 Deems, J. S., Painter, T. H., & Finnegan, D. C. (2013). Lidar measurement of snow depth: A  
606 review. *Journal of Glaciology*, 59(215), 467–479. <https://doi.org/10.3189/2013JoG12J154>
- 607 Ellis, C. R., Pomeroy, J. W., & Link, T. E. (2013). Modeling increases in snowmelt yield and  
608 desynchronization resulting from forest gap-thinning treatments in a northern mountain  
609 headwater basin. *Water Resources Research*, 49(2), 936–949. <https://doi.org/10.1002/wrcr.20089>
- 611 Essery, R., Pomeroy, J. W., Parviainen, J., & Storck, P. (2003). Sublimation of snow from

- 612 coniferous forests in a climate model. *Journal of Climate*, 16(11), 1855–1864. [https://doi.org/10.1175/1520-0442\(2003\)016%3C1855:SOSFCF%3E2.0.CO;2](https://doi.org/10.1175/1520-0442(2003)016%3C1855:SOSFCF%3E2.0.CO;2)
- 613
- 614 Floyd, W. C. (2012). *Snowmelt energy flux recovery during rain-on-snow in regenerating forests* (p. 180) [PhD Thesis, University of British Columbia]. <https://doi.org/https://dx.doi.org/10.14288/1.0073024>
- 615
- 616
- 617 Fryer, B. Y. G. I., Johnson, E. A., Fryer, G. I., & Johnson, E. A. (1988). Reconstructing
- 618 Fire Behaviour and Effects in a Subalpine Forest. *The Journal of Applied Ecology*, 25(3),
- 619 1063–1072. <https://doi.org/https://doi.org/10.2307/2403766>
- 620 Gelfan, A. N., Pomeroy, J. W., & Kuchment, L. S. (2004). Modeling forest cover influences on
- 621 snow accumulation, sublimation, and melt. *Journal of Hydrometeorology*, 5(5), 785–803.
- 622 [https://doi.org/10.1175/1525-7541\(2004\)005%3C0785:MFCIOS%3E2.0.CO;2](https://doi.org/10.1175/1525-7541(2004)005%3C0785:MFCIOS%3E2.0.CO;2)
- 623 Golding, D. L., & Swanson, R. H. (1978). Snow accumulation and melt in small forest openings
- 624 in Alberta. *Canadian Journal of Forest Research*, 8(4), 380–388. <https://doi.org/https://doi.org/10.1139/x78-057>
- 625
- 626 Harder, P., & Pomeroy, J. W. (2013). Estimating precipitation phase using a psychrometric
- 627 energy balance method. *Hydrological Processes*, 27(13), 1901–1914. <https://doi.org/https://doi.org/10.1002/hyp.9799>
- 628
- 629 Harder, P., Pomeroy, J. W., & Helgason, W. D. (2020). Improving sub-canopy snow depth
- 630 mapping with unmanned aerial vehicles: Lidar versus structure-from-motion techniques.
- 631 *Cryosphere*, 14(6), 1919–1935. <https://doi.org/10.5194/tc-14-1919-2020>
- 632
- 633 Harpold, A. A., Krogh, S. A., Kohler, M., Eckberg, D., Greenberg, J., Sterle, G., & Broxton,
- 634 P. D. (2020). Increasing the efficacy of forest thinning for snow using high-resolution
- 635 modeling: A proof of concept in the Lake Tahoe Basin, California, USA. *Ecohydrology*,
- 636 13(4). <https://doi.org/10.1002/eco.2203>
- 637
- 638 Hedstrom, N. R., & Pomeroy, J. W. (1998). Measurements and modelling of snow interception
- 639 in the boreal forest. *Hydrological Processes*, 12(10-11), 1611–1625. [https://doi.org/10.1002/\(SICI\)1099-1085\(199808/09\)12:10/11%3C1611::AID-HYP684%3E3.0.CO;2-4](https://doi.org/10.1002/(SICI)1099-1085(199808/09)12:10/11%3C1611::AID-HYP684%3E3.0.CO;2-4)
- 640 Herwitz, S. R., & Slye, R. E. (1995). Three-dimensional modeling of canopy tree interception
- of wind-driven rainfall. *Journal of Hydrology*, 168(1-4), 205–226. <https://doi.org/10.1016/>

- 641 0022-1694(94)02643-P
- 642 Hijmans, R. J. (2024). *terra: Spatial Data Analysis*. <https://cran.r-project.org/package=terra>
- 643 Katsushima, T., Kato, A., Aiura, H., Nanko, K., Suzuki, S., Takeuchi, Y., & Murakami, S.
- 644 (2023). Modelling of snow interception on a Japanese cedar canopy based on weighing
- 645 tree experiment in a warm winter region. *Hydrological Processes*, 37(6), 1–16. <https://doi.org/10.1002/hyp.14922>
- 646
- 647 Kim, E., Gatebe, C., Hall, D., Newlin, J., Misakonis, A., Elder, K., Marshall, H. P., Hiem-
- 648 stra, C., Brucker, L., De Marco, E., Crawford, C., Kang, D. H., & Entin, J. (2017).
- 649 NASA's snowex campaign: Observing seasonal snow in a forested environment. *2017*
- 650 *IEEE International Geoscience and Remote Sensing Symposium (IGARSS)*, 1388–1390.
- 651 <https://doi.org/10.1109/IGARSS.2017.8127222>
- 652
- 653 Kobayashi, D. (1987). Snow accumulation on a narrow board. *Cold Regions Science and*
- 654 *Technology*, 13(3), 239–245. [https://doi.org/https://doi.org/10.1016/0165-232X\(87\)90005-X](https://doi.org/https://doi.org/10.1016/0165-232X(87)90005-X)
- 655
- 656 Kozak, A., & Kozak, R. A. (1995). Notes on regression through the origin. *Forestry Chronicle*,
- 657 71(3), 326–330. <https://doi.org/https://doi.org/10.5558/tfc71326-3>
- 658
- 659 Langs, L. E., Petrone, R. M., & Pomeroy, J. W. (2020). A  $\delta^{18}\text{O}$  and  $\delta^2\text{H}$  stable water
- 660 isotope analysis of subalpine forest water sources under seasonal and hydrological stress
- 661 in the Canadian Rocky Mountains. *Hydrological Processes*, 34(26), 5642–5658. <https://doi.org/10.1002/hyp.13986>
- 662
- 663 LAStools. (2024). *Efficient LiDAR Processing Software (version 240220, academic)*. <http://rapidlasso.com/LAStools>
- 664
- 665 Lehtonen, I., Kämärainen, M., Gregow, H., Venäläinen, A., & Peltola, H. (2016). Heavy snow
- 666 loads in Finnish forests respond regionally asymmetrically to projected climate change.
- 667 *Natural Hazards and Earth System Sciences*, 16(10), 2259–2271. <https://doi.org/10.5194/nhess-16-2259-2016>
- 668
- 669 Lumbrazo, C., Bennett, A., Currier, W. R., Nijssen, B., & Lundquist, J. (2022). Evaluat-
- ing Multiple Canopy-Snow Unloading Parameterizations in SUMMA With Time-Lapse
- Photography Characterized by Citizen Scientists. *Water Resources Research*, 58(6), 1–22.

- 670        <https://doi.org/10.1029/2021WR030852>
- 671 Lundberg, A., & Hallidin, S. (1994). Evaporation of intercepted snow: Analysis of gov-  
672 erning factors. *Water Resources Research*, 30(9), 2587–2598. <https://doi.org/10.1029/94WR00873>
- 673
- 674 Lundquist, J. D., Dickerson-Lange, S., Gutmann, E., Jonas, T., Lumbrazo, C., & Reynolds, D.  
675 (2021). Snow interception modelling: Isolated observations have led to many land surface  
676 models lacking appropriate temperature sensitivities. *Hydrological Processes*, 35(7), 1–20.  
677 <https://doi.org/10.1002/hyp.14274>
- 678 MacDonald, J. P. J. (2010). *Unloading of intercepted snow in conifer forests* (Master of  
679 Science August, University of Saskatchewan; pp. 0–93). <http://hdl.handle.net/10388/etd-09302010-145706>
- 680
- 681 Mahat, V., & Tarboton, D. G. (2014). Representation of canopy snow interception, unloading  
682 and melt in a parsimonious snowmelt model. *Hydrological Processes*, 28(26), 6320–6336.  
683 <https://doi.org/10.1002/hyp.10116>
- 684 Moeser, D., Stähli, M., & Jonas, T. (2015). Improved snow interception modeling using  
685 canopy parameters derived from airborne LiDAR data. *Water Resources Research*, 51(7),  
686 5041–5059. <https://doi.org/https://doi.org/10.1002/2014WR016724>
- 687 Musselman, K. N., Pomeroy, J. W., & Link, T. E. (2015). Variability in shortwave irradiance  
688 caused by forest gaps: Measurements, modelling, and implications for snow energetics.  
689 *Agricultural and Forest Meteorology*, 207, 69–82. <https://doi.org/https://doi.org/10.1016/j.agrformet.2015.03.014>
- 690
- 691 Natural Resources Canada. (2024). *Precise point positioning*. <https://webapp.csrs-scrs.nrcan-rncan.gc.ca/geod/tools-outils/ppp.php>
- 692
- 693 Nock, C. A., Lecigne, B., Taugourdeau, O., Greene, D. F., Dauzat, J., Delagrange, S.,  
694 & Messier, C. (2016). Linking ice accretion and crown structure: towards a model  
695 of the effect of freezing rain on tree canopies. *Annals of Botany*, 117(7), 1163–1173.  
696 <https://doi.org/https://doi.org/10.1093/aob/mcw059>
- 697 Pfister, R., & Schneebeli, M. (1999). Snow accumulation on boards of different sizes and  
698 shapes. *Hydrological Processes*, 13(14-15), 2345–2355. <https://doi.org/https://doi.org/10.1002/hyp.14274>

- 699 1002/(SICI)1099-1085(199910)13:14/15%3C2345::AID-HYP873%3E3.0.CO;2-N
- 700 Pomeroy, J. W., Brown, T., Fang, X., Shook, K. R., Pradhananga, D., Armstrong, R., Harder,  
701 P., Marsh, C., Costa, D., Krogh, S. A., Aubry-wake, C., Annand, H., Lawford, P., He,  
702 Z., Kompanizare, M., & Moreno, J. I. L. (2022). The cold regions hydrological modelling  
703 platform for hydrological diagnosis and prediction based on process understanding. *Journal  
704 of Hydrology*, 615(128711), 1–25. <https://doi.org/10.1016/j.jhydrol.2022.128711>
- 705 Pomeroy, J. W., Fang, X., & Ellis, C. R. (2012). Sensitivity of snowmelt hydrology in Marmot  
706 Creek, Alberta, to forest cover disturbance. *Hydrological Processes*, 26(12), 1891–1904.  
707 <https://doi.org/10.1002/hyp.9248>
- 708 Pomeroy, J. W., Marsh, P., & Gray, D. M. (1997). Application of a distributed blowing snow  
709 model to the arctic. *Hydrological Processes*, 11(11), 1451–1464. <https://doi.org/10.1002/709>  
710 (sici)1099-1085(199709)11:11%3C1451::aid-hyp449%3E3.0.co;2-q
- 711 Pomeroy, J. W., Parviainen, J., Hedstrom, N., & Gray, D. M. (1998). Coupled modelling of  
712 forest snow interception and sublimation. *Hydrological Processes*, 12(15), 2317–2337. <https://doi.org/10.1002/712>  
713 (SICI)1099-1085(199812)12:15%3C2317::AID-HYP799%3E3.0.CO;2-X
- 714 Pomeroy, J. W., & Schmidt, R. A. (1993). The Use of Fractal Geometry in Modelling Inter-  
715 cepted Snow Accumulation and Sublimation. *Eastern Snow Conference*, 50, 231–239.
- 716 R Core Team. (2024). *R: A Language and Environment for Statistical Computing*. R Foun-  
717 dation for Statistical Computing. <https://www.r-project.org/>
- 718 Rittger, K., Raleigh, M. S., Dozier, J., Hill, A. F., Lutz, J. A., & Painter, T. H. (2020). Canopy  
719 Adjustment and Improved Cloud Detection for Remotely Sensed Snow Cover Mapping.  
720 *Water Resources Research*, 56(6), n/a. <https://doi.org/10.1029/2019WR024914>
- 721 Roesch, A., Wild, M., Gilgen, H., & Ohmura, A. (2001). A new snow cover fraction parame-  
722 terization for the ECHAM4 GCM. *Climate Dynamics*, 17(12), 933–946. <https://doi.org/722>  
10.1007/s003820100153
- 724 Safa, H., Krogh, S. A., Greenberg, J., Kostadinov, T. S., & Harpold, A. A. (2021). Unraveling  
725 the Controls on Snow Disappearance in Montane Conifer Forests Using Multi-Site Lidar.  
726 *Water Resources Research*, 57(12), 1–20. <https://doi.org/10.1029/2020WR027522>
- 727 Satterlund, D. R., & Haupt, H. F. (1967). Snow catch by Conifer Crowns. *Water Resources*

- 728      *Research*, 3(4), 1035–1039. [https://doi.org/https://doi.org/10.1029/WR003i004p01035](https://doi.org/10.1029/WR003i004p01035)
- 729      Schmidt, R. A., & Pomeroy, J. W. (1990). Bending of a conifer branch at subfreezing temper-
- 730      atures: implications for snow interception. *Canadian Journal of Forest Research*, 20(8),
- 731      1251–1253. <https://doi.org/10.1139/x90-165>
- 732      Schmidt, R. A., & Troendle, C. A. (1989). Snowfall into a forest and clearing. *Journal of*
- 733      *Hydrology*, 110(3-4), 335–348. [https://doi.org/10.1016/0022-1694\(89\)90196-0](https://doi.org/10.1016/0022-1694(89)90196-0)
- 734      Smith, C. D. (2007). Correcting the wind bias in snowfall measurements made with a Geonor
- 735      T-200B precipitation gauge and alter wind shield. *87th AMS Annual Meeting*.
- 736      Staines, J., & Pomeroy, J. W. (2023). Influence of forest canopy structure and wind flow
- 737      on patterns of sub-canopy snow accumulation in montane needleleaf forests. *Hydrological*
- 738      *Processes*, 37(10), 1–19. <https://doi.org/10.1002/hyp.15005>
- 739      Storck, P., Lettenmaier, D. P., & Bolton, S. M. (2002). Measurement of snow interception
- 740      and canopy effects on snow accumulation and melt in a mountainous maritime climate,
- 741      Oregon, United States. *Water Resources Research*, 38(11), 1–16. <https://doi.org/10.1029/2002wr001281>
- 742      Troendle, C. A. (1983). The Potential for Water Yield Augmentation From Forest Management
- 743      in the Rocky Mountain Region. *Journal of the American Water Resources Association*,
- 744      19(3), 359–373. <https://doi.org/10.1111/j.1752-1688.1983.tb04593.x>
- 745      Valante, F., David, J. S., & Gash, J. H. C. (1997). Modelling interception loss for two sparse
- 746      eucalypt and pine forests in central Portugal using reformulated Rutter and Gash analytical
- 747      models. *Journal of Hydrology*, 190(1-2), 141–162. [https://doi.org/10.1016/S0022-1694\(96\)03066-1](https://doi.org/10.1016/S0022-1694(96)03066-1)
- 748      Van Stan, J. T., Siegert, C. M., Levia, D. F., & Scheick, C. E. (2011). Effects of wind-
- 749      driven rainfall on stemflow generation between codominant tree species with differing crown
- 750      characteristics. *Agricultural and Forest Meteorology*, 151(9), 1277–1286. <https://doi.org/10.1016/j.agrformet.2011.05.008>
- 751      Varhola, A., Coops, N. C., Weiler, M., & Moore, R. D. (2010). Forest canopy effects on
- 752      snow accumulation and ablation: An integrative review of empirical results. *Journal of*
- 753      *Hydrology*, 392(3-4), 219–233. <https://doi.org/10.1016/j.jhydrol.2010.08.009>
- 754
- 755
- 756

- 757 Vionnet, V., Mortimer, C., Brady, M., Arnal, L., & Brown, R. (2021). Canadian historical  
758 Snow Water Equivalent dataset (CanSWE, 1928–2020). *Earth System Science Data*, 13(9),  
759 4603–4619. [https://doi.org/https://doi.org/10.5194/essd-13-4603-2021](https://doi.org/10.5194/essd-13-4603-2021)
- 760 Watanabe, S., & Ozeki, J. (1964). Study of fallen snow on forest trees (II). Experiment on the  
761 snow crown of the Japanese cedar. *Jap. Govt. Forest Exp. Sta. Bull*, 169, 121–140.
- 762 Wheeler, K. (1987). *Interception and redistribution of snow in a subalpine forest on a storm-*  
763 *by-storm basis*. Western Snow Conference. <http://sites/westernsnowconference.org/PDFs/>  
764 1987Wheeler.pdf

## 765 10 Supporting Information

### 766 10.1 Detailed Description of UAV-Lidar Methodology

767 The REIGL miniVUX-2 laser operates at a near infrared wavelength with a laser beam foot-  
768 print of 0.160 m x 0.05 mm (at 100 m above ground). The accuracy and precision of the  
769 miniVUX-2 is described by REIGL for a lab environment of 0.015 m and 0.01 m respectively  
770 (at 50 m above ground). The miniVUX-2 was configured with a laser pulse repetition rate of  
771 200 kHz, field of view of 360°, scan speed of 31.09 revolutions s<sup>-1</sup> and an angular step width  
772 of 0.0558°, resulting in an expected an average point cloud density of 107 returns m<sup>-2</sup> for each  
773 flight path.

774 Georeferenced point clouds with x, y, and z coordinates for each laser return were generated  
775 following methods outlined by Harder et al. (2020) and Staines & Pomeroy (2023) to reconcile  
776 survey lidar, IMU and GNSS data. A ground-based GNSS system was positioned on a perma-  
777 nent monument during each survey and underwent precise point positioning (PPP) correction  
778 by Natural Resources Canada (2024). Differential GNSS correction of the UAV trajectory was  
779 conducted using the ground-based PPP GNSS observations and the POSPac UAV software.  
780 The UAV-lidar point clouds were then transformed from a sensor referenced coordinate system  
781 to a georeferenced coordinate system (EPSG:32611 - WGS 84 / UTM zone 11N) using the

782 RIEGL Riprocess Software. A vertical offset of up to 6 cm between UAV-lidar flight lines was  
783 observed in the resulting point clouds on March 13<sup>th</sup> and 14<sup>th</sup>, 2024 and was attributed to  
784 IMU position drift. This offset between flight lines was corrected using the BayesStripAlign  
785 software v2.24 (BayesMap Solutions, 2024), which reduces relative and absolute uncertainties  
786 in the vertical elevation of the point cloud using the ground control points (GCP) collected  
787 across the study site using a differential GNSS rover.

788 Quality control, ground classification and calculation of the change in between two UAV-  
789 lidar point clouds was conducted using the LAStools software package (LAStools, 2024). The  
790 ground classification was conducted using the “lasground\_new” function (LAStools, 2024) for  
791 both the pre and post snowfall event point clouds, with a step size set to 2 m and 8 substeps  
792 (ultra\_fine setting). The offset and spike options were set to remove points that are more  
793 than 0.1 m above or below the initial ground surface estimate surface which “lasground\_new”  
794 fits to the last returns. This function is based on an algorithm outlined by Axelsson (2000),  
795 describing the process of making the initial ground surface element.

796 The change in elevation between the two UAV-lidar surveys was interpreted as the increase in  
797 snow accumulation,  $\Delta HS$  over the snowfall event. This change was calculated using a point-  
798 to-grid subtraction method, using the “lasheight” function from the LAStools (2024) software,  
799 as in Deems et al. (2013) and Staines & Pomeroy (2023). The pre snowfall event point cloud  
800 from “lasground\_new” by “lasheight” to construct a “ground” TIN. Subsequently, the height  
801 of each post snowfall event point above the ground TIN, resulting in a point cloud representing  
802  $\Delta HS$ . This point cloud was then converted into a raster of  $\Delta HS$  with a grid cell resolution  
803 of 5 x 5 cm using the “las2dem” function. Further quality control and resampling of the 5 cm  
804 raster of  $\Delta HS$  was conducted using the ‘Terra’ R package (Hijmans, 2024). Areas that were  
805 disturbed over the snowfall event during the in-situ snow survey and values that exceeded the  
806 .999th quantile were removed. To help remove any remaining noise a 25 cm  $\Delta HS$  raster was  
807 generated by computing the median of the 5 cm  $\Delta HS$  values within each 25 cm grid cell.

808 A comparison of UAV-lidar and in-situ snow survey measurements over the March 13–14th  
809 snowfall event and associated error metrics are shown in Figure 13.

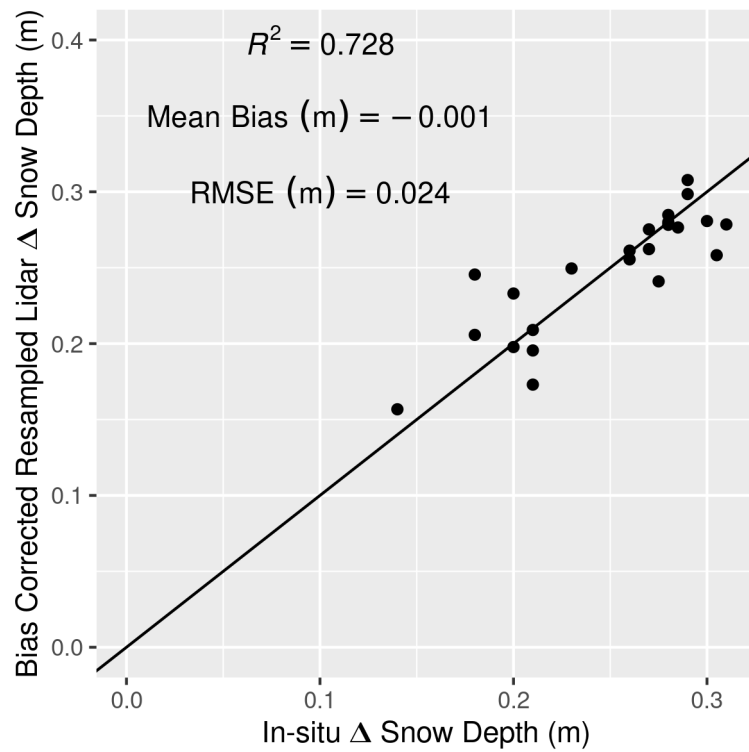


Figure 13: UAV-liar and in-situ snow survey measurements over the March 13–14th snowfall event and associated error metrics.

## 810 10.2 Linear Regression Models Through the Origin

811 Kozak & Kozak (1995) noted, the default  $R^2$  value provided for least squares models forced  
812 through the origin by many statistical packages can be misleading. Therefore, these  $R^2$  values  
813 were adjusted using Equation 10 in Kozak & Kozak (1995) and two statistical tests as described  
814 by Kozak & Kozak (1995) were used to verify whether a no-intercept model (forced through  
815 the origin) was appropriate for this data compared to a with-intercept model. The first test  
816 evaluated if the intercept of the with-intercept was significantly different from zero using p-  
817 value provided by the ‘summary’ function from the ‘stats’ package in R (R Core Team, 2024).  
818 The second test examined if there was a significant difference between the no-intercept and  
819 with-intercept models by testing if the residual sum of squares was different between the no-  
820 intercept and full model, assessed via Equation 15 in Kozak & Kozak (1995). If the first test  
821 indicated a significant difference, and the second did not, the no-intercept model could be  
822 deemed statistically justified (Kozak & Kozak, 1995).